Ann. Geophys., 28, 1703–1722, 2010
www.ann-geophys.net/28/1703/2010/
doi:10.5194/angeo-28-1703-2010

Annales Geophysicae

Empirically modelled Pc3 activity based on solar wind parameters

B. Heilig[1], S. Lotz[2,3], J. Verő[4], P. Sutcliffe[2], J. Reda[5], K. Pajunpää[6], and T. Raita[7]

[1]Tihany Geophysical Observatory, Eötvös Loránd Geophysical Institute, Hungary
[2]Hermanus Geomagnetic Observatory, Hermanus, South Africa
[3]Dept. of Physics and Electronics, Rhodes University, Grahamstown, South Africa
[4]Geodetic and Geophysical Research Institute, Hungarian Academy of Sciences, Sopron, Hungary
[5]Belsk Geophysical Observatory, Polish Academy of Sciences, Poland
[6]Nurmijärvi Geophysical Observatory, Finnish Meteorological Institute, Finland
[7]Sodankylä Geophysical Observatory, University of Oulu, Finland

Received: 11 February 2010 – Revised: 29 June 2010 – Accepted: 2 September 2010 – Published: 22 September 2010

Abstract. It is known that under certain solar wind (SW)/interplanetary magnetic field (IMF) conditions (e.g. high SW speed, low cone angle) the occurrence of ground-level Pc3–4 pulsations is more likely. In this paper we demonstrate that in the event of anomalously low SW particle density, Pc3 activity is extremely low regardless of otherwise favourable SW speed and cone angle. We re-investigate the SW control of Pc3 pulsation activity through a statistical analysis and two empirical models with emphasis on the influence of SW density on Pc3 activity. We utilise SW and IMF measurements from the OMNI project and ground-based magnetometer measurements from the MM100 array to relate SW and IMF measurements to the occurrence of Pc3 activity. Multiple linear regression and artificial neural network models are used in iterative processes in order to identify sets of SW-based input parameters, which optimally reproduce a set of Pc3 activity data. The inclusion of SW density in the parameter set significantly improves the models. Not only the density itself, but other density related parameters, such as the dynamic pressure of the SW, or the standoff distance of the magnetopause work equally well in the model. The disappearance of Pc3s during low-density events can have at least four reasons according to the existing upstream wave theory: 1. Pausing the ion-cyclotron resonance that generates the upstream ultra low frequency waves in the absence of protons, 2. Weakening of the bow shock that implies less efficient reflection, 3. The SW becomes sub-Alfvénic and hence it is not able to sweep back the waves propagating upstream with the Alfvén-speed, and 4. The increase of the standoff distance of the magnetopause (and of the bow shock). Although the models cannot account for the lack of Pc3s during intervals when the SW density is extremely low, the resulting sets of optimal model inputs support the generation of mid latitude Pc3 activity predominantly through upstream waves.

Keywords. Magnetospheric physics (MHD waves and instabilities; Solar wind-magnetosphere interactions)

Correspondence to: B. Heilig
(heilig@elgi.hu)

1 Introduction

Dayside Pc3 (22–100 mHz) geomagnetic pulsations are considered to be the ground counterpart of the so-called 30 s upstream waves (UWs) regularly observed in the Earth's foreshock. These ultra low frequency (ULF) waves are believed to be driven via a wave-particle interaction by the solar wind (SW) ions back-scattered at the bow shock. The resulting waves propagate upstream in the plasma rest frame at the order of the Alfvén speed, but since the SW is super-Alfvénic, UWs are swept back to the magnetosphere by the convection. Under appropriate conditions the UWs are able to penetrate the magnetosheath, propagate across the magnetosphere as compressional mode waves to the turning point where they become evanescent. Consequently, their field penetrates the inner magnetosphere down to the ionosphere, which screens them from the ground and where they are observed as geomagnetic pulsations (Yumoto et al., 1984; Heilig et al., 2007b). During their passage through the magnetosphere these UW originated ULF waves may couple to the Alfvén mode and drive field line resonances where their frequencies match the local eigenfrequencies.

Since the first satellite measurements of the interplanetary medium became available, the connection between surface geomagnetic pulsations and SW parameters has been studied by several authors. The activity, amplitude, power

Published by Copernicus Publications on behalf of the European Geosciences Union.

or occurrence rate of Pc3–Pc5 (Pc4: 7–22 mHz, Pc5: 1.7–7 mHz) pulsations were correlated with different SW and IMF parameters. It was Saito (1964) who showed first that the ground pulsation activity is highly correlated with the SW speed. Some years later Bol'shakova and Troitskaya (1968) found that the occurrence rate of pulsations depends on the direction of the interplanetary magnetic field (IMF), being higher when the IMF is nearly aligned with the Sun-Earth line. Greenstadt and Olson (1976) introduced the term cone angle (ϑ_{Bx}) as a measure of the orientation of the IMF, defined as the angle between the Sun-Earth line and the direction of the IMF. They interpreted the enhanced occurrence rate of Pc3–4s as a consequence of the enhanced probability of their excitation when quasi-parallel structure prevails at the bow shock nose. However, during certain periods the modulation of Pc3 amplitudes did not follow the expected behaviour. Miyake et al. (e.g., 1987), who compared the Suisei probe's SW speed measurements with Pc3 amplitudes observed at Onagawa ($L = 1.3$) found a decreasing correlation during late 1985 (namely $R = 0.79$ in October, but $R = 0.57$ in December). Yedidia et al. (1991) carried out a similar correlation analysis between ground Pc3 power recorded at L'Aquila and SW speed measured by the IMP-8 satellite, based on a full year (1985) data set and found a similar trend, although their correlation coefficients were higher (namely $R = 0.89$ in October, but $R = 0.75$ in December). The total disappearance of Pc3 activity during the famous low-density solar wind event (LDA – low-density anomaly) on 11 May 1999, which became known as "the day the solar wind almost disappeared", again attracted attention to this unsolved problem. Although during this LDA the SW speed was close to average conditions ($\sim$350 km s^1) and the cone angle was favourable ($\sim$40°) for the generation of ground Pc3s, Pc3 activity could not be observed in the magnetosphere or on ground (Le et al., 2000a,b).

Some authors (e.g., Wolfe, 1980; Wolfe and Meloni, 1981; Verő, 1980; Yedidia et al., 1991; Chi et al., 1998; Chugunova et al., 2007) tried to refine the relationship between SW conditions and pulsation activity by adding other interplanetary parameters (e.g. plasma number density, IMF components, clock angle, mass flux, dynamic pressure, kinetic energy flux density, Akasofu's ϵ parameter) to their analyses, but with limited success. In most of the cases a simple linear regression analysis was executed, while Wolfe in a series of papers (Wolfe, 1980; Wolfe and Meloni, 1981) applied a more complex model consisting of a linear combination of the considered variables estimated by multiple linear regression analysis.

In this work we re-investigate the SW control of geomagnetic pulsation activity. Case studies and the results of a statistical analysis based on high resolution magnetometer data recorded with the MM100 meridional array are presented. We demonstrate for the first time the dependence of ground Pc3-Pc4 amplitudes on the standoff distance of the magnetopause (bow shock) and on upstream Alfvén Mach number (M_A). In light of these results we discuss the behaviour of Pc3s during LDAs. Our results support UW activity as the dominant source of dayside mid-latitude Pc3s.

2 Data and analysis

2.1 MM100 ground magnetometer array

MM100 is the acronym for a quasi-meridional magnetometer array established in September of 2001 for pulsation studies. The array consists of Finnish, Estonian, Polish, Slovak and Hungarian stations ranging from high to mid latitudes ($L = 6.1$ to $L = 1.8$) distributed along the 100° magnetic meridian (see Table 1). The instruments used are high resolution (1–10 pT) fluxgate or torsion photoelectric magnetometers with GPS synchronised timing, sampled at 1 Hz (Heilig et al., 2007a,b).

In this study a Pc3 index (Pc3ind) was used to characterise the pulsation activity at the ground stations. Pc3ind is defined as the root-mean-square (rms) value of the bandpass (22–100 mHz) filtered time series of the H-component expressed in pT. Pc3 amplitude indices were calculated for every hour for the period 2001–2007 in the case of Tihany (THY, $L = 1.8$) data. For the other MM100 stations only the 2003 data were used. Here we mostly present the results extracted from the THY data set, but some results of the analyses of pulsations recorded at other MM100 stations are also shown.

We used the solar zenith angle to account for the local time variation of pulsation activity. Solar zenith angle χ, which is the angle between the local zenith and the line of sight to the Sun, is a function of geographic position and local time. The solar zenith angle was calculated for all MM100 stations for all hours.

2.2 Solar wind data

The IMF and SW plasma data used, are from the OMNI2 database where all data are corrected for convection delay. OMNI2 data are publicly available at GSFC's OMNIweb server: omniweb.gsfc.nasa.gov/html/ow_data.html. These data are used in the geocentric solar magnetospheric (GSM) system with a time resolution of 1 h in the analyses and with 1 min resolution for Figs. 1 and 2.

The OMNI2 IMF and SW parameters used in this study are: IMF strength ($B_{\rm imf}$), the x-component of the IMF (B_x), SW speed ($v_{\rm sw}$) and its x-component (v_x), SW plasma (proton) density ($N_{\rm p}$), the ratio of the number of the alpha particles and protons ($q_{\rm He}$), Alfvén Mach number ($M_{\rm A} = v_{\rm sw}/v_{\rm A}$, where $v_{\rm A} = B_{\rm imf}/\sqrt{\mu_0 N_i m_{\rm p}}$ is the Alfvén speed, μ_0 is the vacuum permeability, $N_i = (1 + 4q_{\rm He})N_{\rm p}$ assuming 4% He when $q_{\rm He}$ is not available, and dynamic pressure ($p_{\rm dyn} = N_i m_{\rm p} v_{\rm sw}^2$ or $1.2 N_{\rm p} m_{\rm p} v_{\rm sw}^2$ depending on the availability of $q_{\rm He}$).

Table 1. Stations of the MM100 pulsation recording array.

Station Name	Operating Institute	IAGA Code	Geographic Coordinates Latitude N	Geographic Coordinates Longitude E	AACGM Coordinates (2001) Latitude N	AACGM Coordinates (2001) Longitude E	McIlwain L shell
Kilpisjärvi	IMAGE	KIL	69.02°	20.79°	66.10°	104.00°	6.09
Sodankylä	IMAGE	SOD	67.37°	26.63°	64.16°	107.46°	5.26
Oulujärvi	IMAGE	OUJ	64.52°	27.23°	61.23°	106.31°	4.32
Hankasalmi	IMAGE	HAN	62.30°	26.65°	59.01°	104.78°	3.77
Nurmijärvi	IMAGE	NUR	60.52°	24.65°	57.23°	102.34°	3.41
Tartu	IMAGE	TAR	58.26°	26.46°	54.48°	103.04°	3.01
Suwalki	PAS	SUW	54.01°	23.18°	50.34°	98.83°	2.45
Belsk	PAS	BEL	51.83°	20.80°	48.01°	96.15°	2.23
Hurbanovo	SAS	HRB	47.87°	18.18°	43.56°	92.86°	1.90
Nagycenk	ELGI-USGS	NCK	47.63°	16.72°	43.27°	91.53°	1.89
Farkasfa	ELGI-USGS	FKF	46.91°	16.31°	42.43°	91.00°	1.84
Tihany	ELGI-USGS	THY	46.90°	17.89°	42.44°	92.39°	1.84

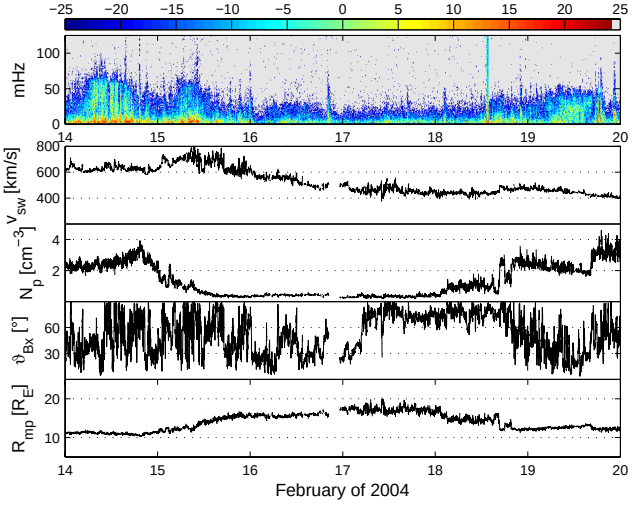

Fig. 1. LDA (15 February 14:00 UT–17 February 22:00 UT, 2004) at the trailing edge of a fast flow. The upper panel shows the dynamic power spectral density for THY, the next four panels the OMNI2 1-min resolution SW parameters, namely, v_{sw}, N_p, ϑ_{Bx} and R_{mp} for the interval between 14–19 February 2004.

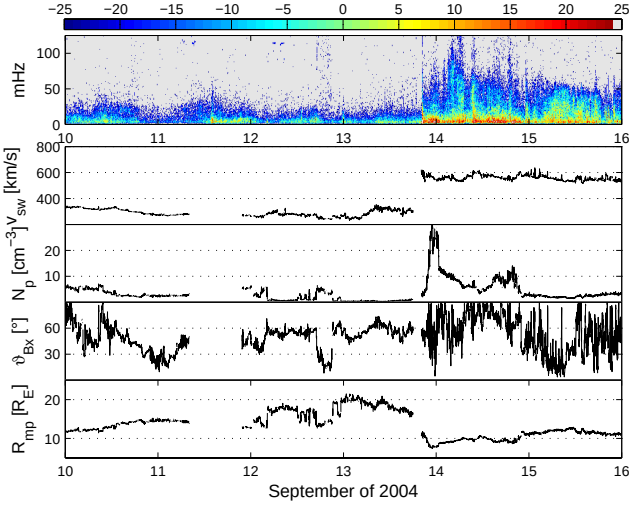

Fig. 2. SAE (13 September 00:00 UT–08:00 UT, 2004) embedded in a slow wind period prior to a fast solar wind stream arriving at 21:00 UT. Same format as Fig. 1.

Other parameters were calculated from OMNI2 data. IMF cone angle is defined as $\vartheta_{Bx} = \arccos(|B_x|/B_{imf})$. Magnetopause standoff distance was calculated assuming a constant dipolar geomagnetic field using the formula $R_{mp} = 110.2(N_p v_x^2)^{-1/6}$ (derived in a similar way as in Kivelson and Russell, 1995, page 172). In this formula N_p, v_x, and R_{mp} are given in cm^{-3}, km s^1, and R_E, respectively. We calculated the magnetosonic Mach number as $M_{ms} = v_{sw}/\sqrt{v_A^2 + v_s^2}$, where $v_s = \sqrt{\gamma k_B (T_p + T_e)/(m_p + m_e)}$ is the sonic speed, γ is the polytropic index (here = 5/3), k_B is the Boltzmann constant, T_p and T_e are the proton and electron temperatures, m_p and m_e are the proton and electron masses. In this study $(T_p + T_e)/(m_p + m_e)$ was approximated by $2T_p/m_p$.

3 Observations

3.1 Low-density anomalies and sub-Alfvénic events

Usmanov et al. (2005) listed 23 low-density anomalies, i.e. intervals when the SW density, $N_p \leq 0.3\,\mathrm{cm}^{-3}$, and 11 sub-Alfvénic ($M_A \leq 1$) periods inferred from the OMNI2 dataset between 1963 and 2003. Here we updated and extended Usmanov's list adding LDAs and sub-Alfvénic events (SAEs) observed from 2004 to 2008. These are shown in Tables 2 and 3, respectively. Events with less than 24 h separation were considered a single event. The first three columns give the start of the event (year, day of the year, and UT in hours). The duration of an event given in hours is the number of hourly intervals during the event for which the low-density

Table 2. Low-density ($N_p \leq 0.3\,cm^{-3}$) anomalies in OMNI2 data (2001–2008). Asterisks (*) indicate that a part of the hourly values is missing.

year	DOY	UT h	dur. h	B_{imf} nT	N_p cm^{-3}	v_{sw} $km\,s^{-1}$	p_{dyn} nPa	M_A	ϑ_{Bx} deg.	Pc3ind pT
2001	12	19	1	6.8	0.3	324	0.06	1.3	44	–/n.a.
2001	120	18	2	4.8	0.3	434	0.18	2.5	16	–/7*
2001	151	11	2	6.6	0.3	360	0.10	1.4	48	9/9
2001	251	19	5	6.3	0.2	391	0.05	1.3	34	–/12*
2001	311	7	1	8.0	0.3	651	0.38	2.2	34	11/11
2002	79	11	3	13.3	0.3	400	0.08	0.8	63	57/57*
2002	143	22	42	10.3	0.2	589	0.12	1.1	39	8/7
2002	200	17	6	17.1	0.2	781	0.26	1.1	29	9/15
2003	187	22	2	7.1	0.3	577	0.20	2.3	46	–/18
2004	46	21	14	6.2	0.3	495	0.15	2.2	46	7/9
2004	205	2	5	13.8	0.2	633	0.16	1.0	76	–/67
2004	257	10	1	11.0	0.3	318	0.06	0.8	62	9/9
2005	20	1	4	5.4	0.3	758	0.32	4.1	63	–/30
2006	322	20	3	9.2	0.3	392	0.08	1.1	70	–/7
2006	324	14	2	7.3	0.3	323	0.07	1.2	50	7/7

Table 3. Sub-Alfvénic ($M_A \leq 1$) events in OMNI2 data (2001–2008). Asterisks (*) indicate that a part of the hourly values is missing.

year	DOY	UT h	dur. h	B_{imf} nT	N_p cm^{-3}	v_{sw} km/s	p_{dyn} nPa	M_A	ϑ_{Bx} deg.	Pc3ind pT
2001	170	12	1	16.0	0.6	398	0.23	1.0	52	8/8
2001	251	21	1	6.2	0.1	395	0.03	1.0	36	–/n.a.
2002	79	3	11	14.5	0.5	377	0.16	0.9	64	21/18*
2002	144	11	24	10.1	0.1	492	0.07	0.9	48	7/7
2002	200	17	5	18.1	0.2	792	0.25	1.0	27	9/11
2003	275	5	2	18.1	1.4	302	0.24	1.0	48	8/8
2003	302	18	1	44.5	0.8	953	1.45	1.0	31	–/152
2004	205	3	1	13.9	0.2	630	0.16	1.0	72	–/31
2004	256	6	13	10.6	0.4	280	0.07	0.9	56	8/7
2006	322	21	1	9.2	0.2	390	0.06	0.9	68	–/7

condition was satisfied. The next six columns provide the average B_{imf}, N_p, v_{sw}, p_{dyn}, M_A and ϑ_{Bx} of the events. In the last column the average Pc3inds are given in pT. The values separated by "/" are calculated from daylight hours/all hours data, respectively.

Usmanov et al. (2005) interpreted low-density anomalies as rarefaction of SW plasma at the trailing edge of a high speed stream from a coronal hole. We found an example (September 2004), when the SAE is connected to the leading edge of a fast stream. Table 3 clearly demonstrates that sub-Alfvénic flows are not necessarily embedded in low-density events. Sometimes a relatively high value of the IMF strength ($> 10-20$ nT, the actual limit depends on both v_{sw} and N_p) can also lead to a low M_A, especially on 6 June 1979 (doy 157, $B_{imf} = 36$ nT, event not shown in Table 3) and on 29 October 2003 (doy 302, $B_{imf} = 44.5$ nT, $v_{sw} = 953\,km\,s^{-1}$, $N_p = 0.8\,cm^{-3}$). During the latter event, the largest among the Halloween storms of 2003, both B_{imf} and v_{sw} had extreme values; B_{imf} was close to the largest value (55.8 nT) recorded since the beginning of the space era (Veselovsky et al., 2010).

3.2 The lack of Pc3 pulsations during LDAs and SAEs

Below we present two examples of the disappearance of Pc3 (22–100 mHz) pulsations during an LDA and a SAE.

Figure 1 presents a long LDA that lasted from 15 February 2004 at 21:00 UT until 17 February 2004 at 22:00 UT. The upper panel shows the dynamic power spectrum observed at THY for the six day long interval (14–19 February 2004). The other four panels present the variation of the SW conditions, namely the time series of v_{sw}, N_p, ϑ_{Bx} and R_{mp}. Before the LDA N_p was moderately low ($> 2\,cm^{-3}$), v_{sw} was moderately high ($\approx 600\,km\,s^{-1}$) resulting in a close to

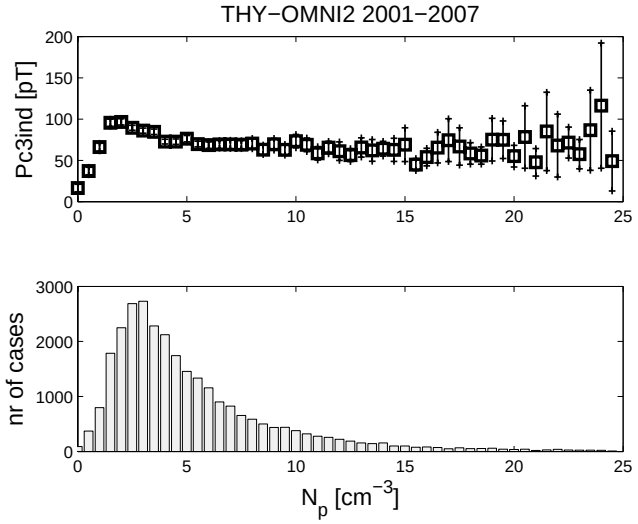

Fig. 3. THY Pc3 index (2001–2007) vs. proton number density (upper panel) with 95% confidence intervals, and the histogram of N_p (lower panel).

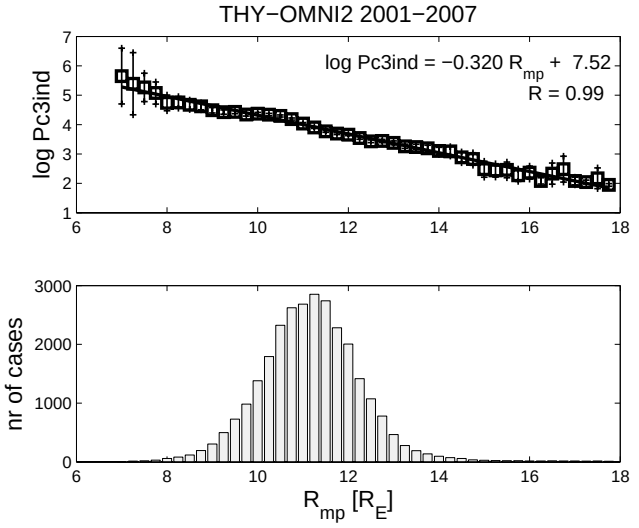

Fig. 4. THY log Pc3 index vs. standoff distance of the magnetopause (2001–2007). Same format as Fig. 3, but upper panel also includes the fitted curve, its equation, and the correlation coefficient of the fitted curve and the interval means.

average R_{mp}, while ϑ_{Bx} was highly fluctuating. Under these conditions moderate Pc3 activity was observed at THY on the ground. On 15 February, at the trailing edge of the fast wind flow N_p started to decrease, while v_{sw} remained high, resulting in a high R_{mp} by the end of the day. In the meanwhile the Pc3 ULF activity decreased but it was still observable. The LDA started on this day at 21:00 UT. On the following two days, during the LDA there was no significant ULF activity in the Pc3 band. Usual ULF activity returned on 19 February. The solar wind was super-Alfvénic during the whole event.

Figure 2 shows an example of a SAE. This event started on 12 September, 2004 at 06:00 UT and finished on 13 September at 08:00 UT. Before and during the SAE v_{sw} was low ($\approx 300\,\mathrm{km\,s^{-1}}$), N_p dropped from low ($2.5\,\mathrm{cm^{-3}}$) to extremely low ($< 1\,\mathrm{cm^{-3}}$), ϑ_{Bx} varied between low and moderately high values. R_{mp} increased up to 20 R_E during the SAE, and of course, the SW flow was sub-Alfvénic. The ULF activity was low throughout the whole slow wind interval, and was the lowest during and immediately after the SAE. The situation changed on the night of 13 September when a fast wind stream with a shock front arrived, producing a pressure pulse. R_{mp} decreased down to 7.5 R_E. On the following day intense activity in the Pc4 band and an increased activity in the Pc3 band were observed.

In these cases the Pc3 activity is practically missing from the dayside and from the nightside, too. Similarly, Le et al. (2000a) found the magnetosphere much quieter than usual during an event in May 1999 ("the day the solar wind almost disappeared").

These experiences, in accordance with previous ones, suggest that there should be a strong connection between the plasma density of the SW and the ULF wave activity both in the foreshock and in the magnetosphere, as well as on the ground.

4 Statistical analysis

4.1 The role of solar wind plasma density

The SW speed control of Pc amplitudes is the most widely known relation between ground pulsation activity and the properties of the interplanetary medium, first realised by Saito (1964). The dependence of Pc3 amplitudes on N_p beside other SW parameters was also investigated by several authors (Wolfe and Meloni, 1981; Yedidia et al., 1991; Chugunova et al., 2007), but the negative correlation found was always less significant than the correlation with v_{sw}, e.g. $R = -0.16$ compared to $R = 0.56$ observed at Pittsburgh ($L = 3.5$) by Wolfe and Meloni (1981) in the summer of 1975, or $R = -0.62$ compared to $R = 0.86$ found by Yedidia et al. (1991) based on a year-long data set of hourly average integrated (Pc3 band) log power observed at L'Aquila ($L = 1.5$) in 1985. This result was usually attributed to the fact that the N_p and v_{sw} are not independent variables, but they themselves have a negative correlation (e.g. Hundhausen et al., 1970; Kulcar, 1988; McComas et al., 2000; Veselovsky et al., 2010).

Wolfe and Meloni (1981) applied multiple linear regression (MLR) analyses on dayside integrated (17–33 mHz band) log power of the ground H-signal to find the SW quantities which principally control the level of Pc3 activity. They concluded that, beside v_{sw} ($R = 0.56$) and ϑ_{Bx} ($R = -0.35$),

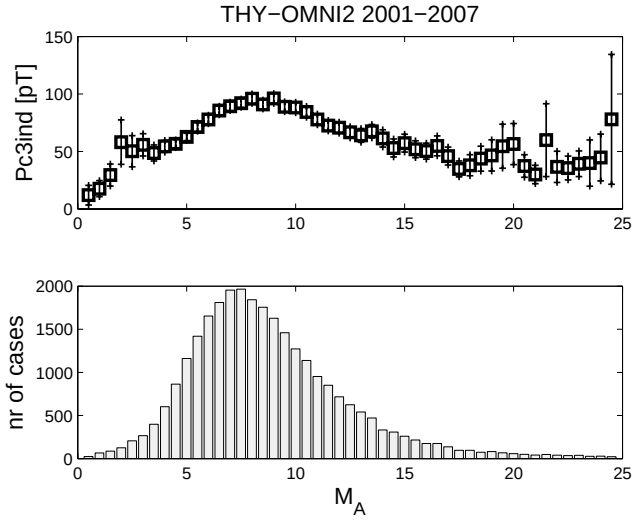

Fig. 5. THY Pc3 index vs. Alfvén Mach number (2001–2007). Same format as Fig. 3.

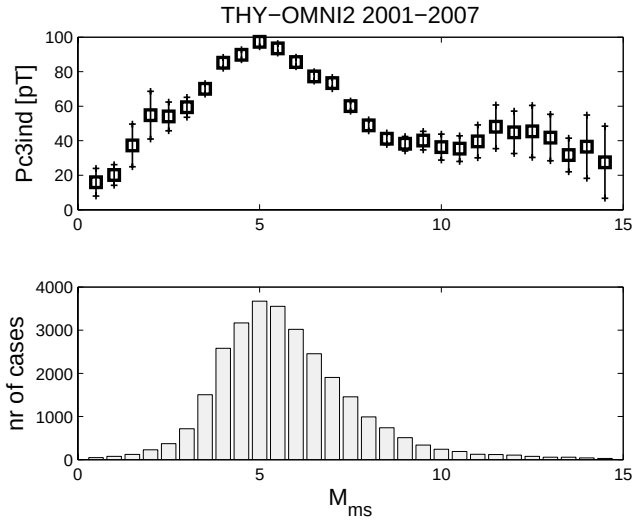

Fig. 6. THY Pc3 index vs. magnetosonic Mach number (2001–2007). Same format as Fig. 3.

N_p is the third in importance of the eight SW parameters investigated, in spite of the fact that in itself it had practically no correlation ($R = -0.16$) with Pc3 activity. As an alternative to N_p the kinetic energy flux density ($1/2 N_\mathrm{p} m_\mathrm{p} v_\mathrm{sw}^3$) yielded a relatively high correlation of $R = 0.36$. However, it is not clear from that work whether the inclusion of N_p in the MLR analyses improved the correlation or not, since it was the first quantity chosen in the analysis, and the others subsequently added one by one. The maximum correlation achieved was $R = 0.70$ when all eight SW parameters (N_p, $1/2 N_\mathrm{p} m_\mathrm{p} v_\mathrm{sw}^3$, B_imf, $B_{x\mathrm{gsm}}$, $B_{y\mathrm{gsm}}$, $B_{z\mathrm{gsm}}$, ϑ_{Bx}, v_sw) were included in the MLR.

Here, we demonstrate first how the THY Pc3 amplitudes (2001–2007 hourly means) are linked to OMNI2 N_p (Fig. 3) and other N_p dependent SW parameters, such as R_mp (Fig. 4), M_A (Fig. 5), M_ms (Fig. 6) and p_dyn (Fig. 7). Figures 3 to 7 present these relations in the same format. In each figure the upper panel shows the dependence of Pc3ind on the chosen parameter together with the 95% confidence intervals as error bars, while in the lower panel the histogram of the occurrence frequency of the parameter considered is displayed. It can be clearly seen that all the enumerated SW parameters have some connections to ground Pc3 activity. The level of Pc3 activity dramatically drops if the N_p is less than $2\,\mathrm{cm}^{-3}$ (Fig. 3) or the dynamic pressure is under 2 nPa (Fig. 7), but these parameters have no or much less influence above these thresholds. Pc3 activity maximises around the average Alfvén and average magnetosonic Mach number, and rapidly vanishes toward low Mach numbers (Fig. 5 and 6). The only N_p dependent parameter that has a significant monotonic influence on Pc3ind in the whole value-range is the standoff distance of the magnetopause (Fig. 4); the further the magnetopause stands from the Earth, the lower the ground Pc3 activity.

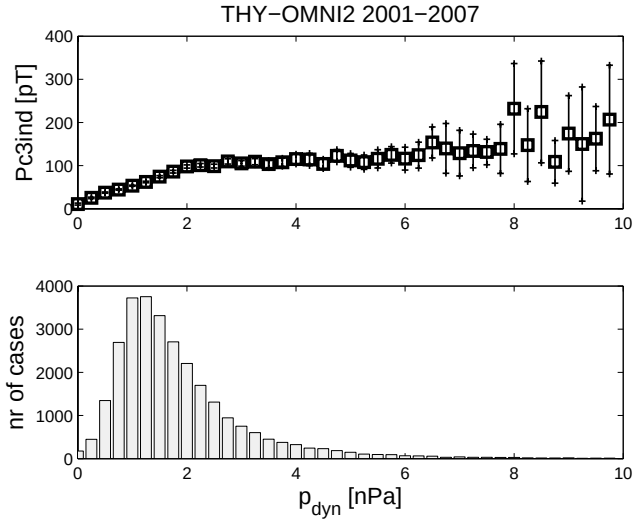

Fig. 7. THY Pc3 index vs. dynamic pressure (2001–2007). Same format as Fig. 3.

We note here, that except for the N_p dependence itself, which was previously noted by Verő (1980) and Chugunova et al. (2007), all relationships between the Pc3 activity and the N_p dependent parameters are presented here for the first time. The presented dependences of Pc3ind on N_p, R_mp, M_A, M_ms show that any or all of them could be responsible for the disappearance of Pc3s during LDAs and SAEs.

4.2 Separation of the influences of solar wind parameters

The SW parameters are not independent of each other. The anti-correlation between the SW plasma density and bulk speed is the most widely known relationship of this type. To

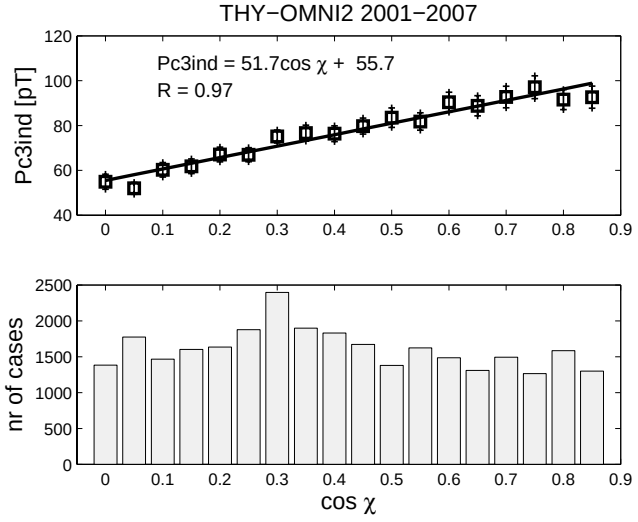

Fig. 8. THY Pc3 index vs. the cosine of the solar zenith angle (2001–2007). Same format as Fig. 4.

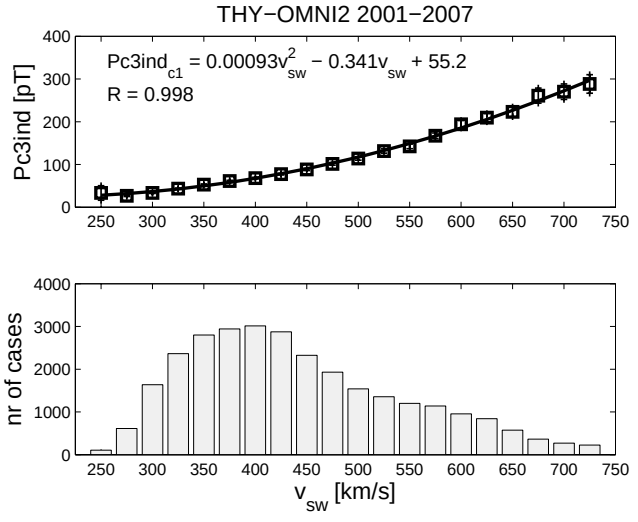

Fig. 9. Normalised (c1) THY Pc3 index vs. solar wind speed (2001–2007). Same format as Fig. 4.

avoid the interference of the considered parameters in our analysis, we investigated the contribution of the parameters to Pc3ind successively. The relation between Pc3ind and the parameter considered was estimated by the best-fitting polynomial. Then based on this relation Pc3ind was normalised to a typical value of the parameter.

In the first step the average hourly Pc3inds versus the cosine of the solar zenith angle (χ) were binned to account for the daily variation of the Pc3 activity. The solar zenith angle was chosen as the first parameter, because of its obvious independence of all SW parameters. The relation between Pc3ind and χ shown in Fig. 8 can be well ($R = 0.97$) approximated by a linear equation. Figure 8 has the same format as Fig. 4. The linear equation was then used to normalise all Pc3ind values to $\chi = 30°$ (Pc3ind$_{c1}$).

In the second step the normalised activity indices were plotted against the SW speed (Fig. 9). The resulting relation was approximated ($R = 0.998$) by a quadratic formula. This is very similar to what is observed without normalisation (Pc3ind $= 0.00070 v_{\rm sw}^2 - 0.248 v_{\rm sw} + 39.9\,pT$, $R = 0.999$); the only significant difference is that the normalisation increased Pc3ind values by 27–30% because of our choice of $\chi = 30°$ as reference level in the previous step. For the second normalisation 400 km s^{-1} was taken as reference level.

The dependence of the twice normalised indices (Pc3ind$_{c2}$) on the standoff distance of the magnetopause ($R_{\rm mp}$) was considered next. From the result presented in Fig. 10 it is seen that $R_{\rm mp}$ is closely related to ground Pc3 activity and that this relation is not a simple consequence of $v_{\rm sw}$ dependence, but is an independent factor. The dependence of the normalised Pc3 amplitudes on $R_{\rm mp}$ can be modelled by a linear equation ($R = 0.98$) in the 8-14 $R_{\rm E}$ range. It is different from the exponential decay found without normalisations (Fig. 4). For the third normalisation a reference level at $R_{\rm mp} = 10.5\,R_{\rm E}$ was chosen (Pc3ind$_{c3}$).

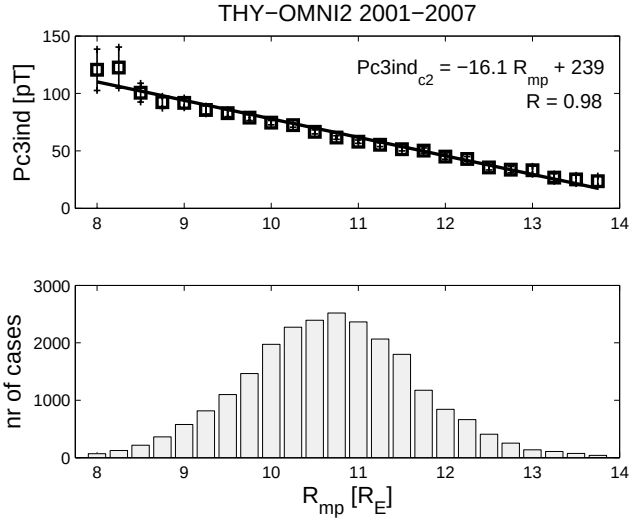

Fig. 10. Normalised (c2) THY Pc3 index vs. standoff distance of the magnetopause (2001–2007). Same format as Fig. 4.

Figure 11 shows that even after all these normalisations the activity is strongly dependent on the cone angle. The maximum is at 0° and a linear dependence ($R = 0.99$) on $\cos^2\vartheta_{Bx}$ was found. It proves that the cone angle control is not just a consequence of the interrelation of the SW parameters. However, this result is different from what is found without normalisation. For comparison, the dependence of the observed Pc3ind on $\cos^2\vartheta_{Bx}$ can not be described by a linear equation, but by a quadratic formula (Pc3ind $= -147.20\cos^4\vartheta_{Bx} + 185.56\cos^2\vartheta_{Bx} + 42.0$ pT, $R = 0.97$) with a maximum at 37°. This is in agreement with the theoretical prediction of Kovner et al. (1976), who found that the ion-cyclotron instability near the nose of the bow shock is the most efficient when the cone angle is around 30°.

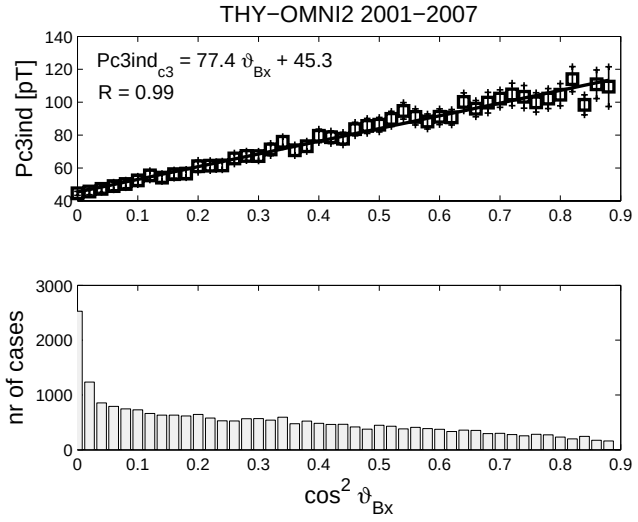

Fig. 11. Normalised (c3) THY Pc3 index vs. cosine of the IMF cone angle (2001–2007). Same format as Fig. 4.

The order of normalisation and the reference levels chosen are all arbitrary. Since three of the four parameters considered here are not independent of each other, the results of the 2nd to 4th steps are determined by the particular order of steps chosen. In this section we had only one goal, to demonstrate that all the considered interdependent parameters have their own influence on ground Pc3 activity.

The analysis of partial correlations yields another approach to verify the interdependence of SW parameters and to separate their influences on Pc3ind. Partial correlation, i.e. correlation between two random variables, with the effect of a set of controlling random variables removed, was computed for selected parameter pairs.

The coefficient of the anti-correlation between N_p and v_{sw} was calculated at $R = -0.38$ for the whole period. This is consistent with the findings of Kulcar (1988), who correlated v_{sw} and N_p averaged in 50 km s^{-1} wide SW speed bins, and found that the correlation varied from $R = -0.36$ to -0.68 during solar cycles 20 and 21, with stronger correlation at sunspot minima. The partial correlation of N_p and v_{sw} after removing the effect of the IMF strength is somewhat stronger, i.e. $R = -0.46$, while the variation of ϑ_{Bx} had no influence on this correlation. The anti-correlation between v_{sw} and R_{mp} was weaker ($R = -0.18$); however, after removing the effect of N_p, it increased to $R = -0.59$. This was expected, because R_{mp} is a function of v_{sw} and N_p. The correlation between N_p and R_{mp} was even stronger, $R = -0.64$, and after removing the effect of v_{sw} it further increased to $R = -0.77$. There was no significant correlation found, however, between ϑ_{Bx} and other SW parameters.

For the derivation of partial correlation coefficients between Pc3ind and different parameters only dayside values ($\chi < 90°$) were considered. The correlation coefficient between Pc3ind and v_{sw} was the highest, $R = 0.60$. Choosing N_p as a control parameter, the partial correlation is nearly the same, $R = 0.62$. The correlation between Pc3ind and N_p was rather low ($R = -0.06$), which explains why former authors usually did not take N_p into account in their correlation analyses. The partial correlation with v_{sw} as the control variable is somewhat higher, $R = 0.24$, but still does not suggest a strong connection. But if we select R_{mp} as control variable, we get a more significant anti-correlation, $R = -0.38$, suggesting that R_{mp} has a more important role, than N_p itself. Indeed, the anti-correlation strength between Pc3ind and R_{mp} is $R = -0.35$, which increases to $R = -0.50$ when removing the effect of N_p. If we use both N_p and v_{sw} as control parameters, the partial correlation coefficient drops to $R = -0.22$ meaning that the joint use of R_{mp} and N_p in a multiple regression implicitly bears a part, but not all of the information that v_{sw} contains.

Wolfe (1980) found that hourly mean v_{sw} and ϑ_{Bx} had significant correlation ($R = 0.34$) between 17–21 July 1975, while this behaviour ceased ($R = -0.08$) two weeks later (28 July–2 August), and concluded that these parameters can be considered as independent. Comparing these two time intervals they also found that the correlation of the log power (band integrated, 17–33 mHz, i.e. lower Pc3 range) of daytime ground pulsations observed at Pittsburgh ($L = 3.5$) with v_{sw} increased (from $R = 0.28$ to $R = 0.68$) between the two intervals, while the log power – ϑ_{Bx} relation remained unchanged ($R = -0.40$ and $R = -0.38$). They concluded that the higher ϑ_{Bx} values at higher v_{sw} in the first interval eroded the log power – v_{sw} relation.

4.3 Multiple regression analysis

A MLR analysis was carried out with a carefully chosen set of variables. We started with the parameter found to have the most significant influence on the Pc3 indices, the SW speed, and added the others step by step. It was decided not to model Pc3ind by a simple linear combination of the parameters, but by the product of the parameters (p_i) raised to an unknown power (α_i):

$$\text{Pc3ind} = C \cdot p_1^{\alpha_1} \cdot p_2^{\alpha_2} \cdot \ldots \cdot p_n^{\alpha_n} + D, \quad (1)$$

where C and D are unknown constants. A similar formulation was used by Verő (1980) to determine the exponent of v_{sw} in the expression $A = C \cdot v_{sw}^{\alpha}$ by a simple regression analysis. We chose this formulation for two reasons: 1. The approach based on the exponents enables one to draw conclusions on the possible role of parameters that can be expressed as the product of the investigated ones but which are not investigated directly, such as kinetic energy flux density ($1/2 N_p m_p v_{sw}^3$). 2. Supposing that there is more than one parameter that affects the dayside activity of ULF waves coming from the same source, the joint effect (e.g. efficiency of generation, transparency of different plasma regions, attenuation, the role of the ionosphere) of these parameters will

Table 4. Results of the simple regressions (Pc3ind $= Cp^{\alpha} + D$), and the correlation coefficient, R. Parameters v_{sw}, N_p, B, R_{mp}, p_{dyn} and D are in km s^{-1}, cm^{-3}, nT, R_E, nPa and pT, respectivly.

v_{sw}	2.51							
N_p		−0.07						
B			0.52					
$\cos\vartheta_{Bx}+2$				2.63				
$\cos\chi$					0.18			
R_{mp}						−3.74		
p_{dyn}							0.60	
M_A								0.01
$\log_{10}C$	−4.87	2.07	1.43	0.77	2.00	5.73	1.67	1.73
D	6	−29	9	9	−7	10	10	23
R	0.60	0.06	0.22	0.23	0.16	0.35	0.35	0.00

be better described by the product of the controlling parameters rather than by their sum. The sum would better fit cases where multiple independent sources are acting simultaneously.

Equation (1) can be realised through linear regression analysis by the linear combination of the logarithms of the parameters considered:

$$\log \text{Pc3ind} = c + \alpha_1 \log p_1 + \alpha_2 \log p_2 ... + \alpha_n \log p_n, \quad (2)$$

where c is an unknown constant. Since C and D in Eq. (1) are constants they do not modify the correlation between the LHS and RHS of Eq. (1), hence D can be taken as zero in Eq. (2); however, both C and D have to be determined later for the models of Pc3ind. This can be done by a simple linear regression between Pc3ind and the MLR model (based on Eq. 2) result.

Since the logarithm is not defined for non-positive values we added 2 to the cosine of the cone angle to avoid zero as an argument when $\vartheta_{Bx} = 90°$. By choosing a value 2 we also avoided the close to zero arguments that would produce outstanding negative values distorting the result of the regression analysis. Of course, 2 is an arbitrary choice, and the actual value of this constant influences the resulting exponent. However, we found that the correlation coefficient does not change significantly if we increase this constant. All other parameters have positive values, including the cosine of the solar zenith angle on the dayside.

All available pulsation data recorded at Tihany between 2001–2007 and the corresponding available OMNI2 SW data together provided 28 562 samples (hourly means), which were used in these analyses to derive the presented Pc3ind models.

The results of the simple regression analyses are summarised in Table 4. A column of the table contains the exponent α in the row of the parameter p considered, the constants C and D from the equation Pc3ind $= Cp^{\alpha} + D$, and the correlation coefficient R. The different columns correspond to linear regressions for the different parameters. For example, the first column shows that Pc3ind $= 10^{-4.87} v_{sw}^{2.51} + 6$ pT, and $R = 0.60$. This is in accordance with previous results showing that the most important factor controlling ground Pc3 activity is the SW speed. The exponent of v_{sw} is close to 5/2. This is in agreement with the findings of Verő (1980), who found that the exponent is greater than 2 for periods less than 30 s, about 2 for periods around 30 s, and less for longer periods.

Again in accordance with previous studies (e.g. Verő, 1980; Chugunova et al., 2007) there is no correlation between N_p and Pc3 activity (Table 4, second column). This is shown both by the low correlation coefficient and the close to zero exponent. Although it was demonstrated that in the lowest range of values ($N_p < 2$ cm^{-3}) N_p does have a strong effect on Pc3ind (Fig. 3), there is no dependence above this threshold. The situation is similar for M_A (Fig. 5), where we can find correlation in some intervals, but when the whole range of possible values are taken into account, the correlation coefficient is close to zero. On the other hand ϑ_{Bx}, B_{imf}, R_{mp} and p_{dyn} all seems to have some influence on Pc3ind (Table 4). The correlation in the case of R_{mp} is an anti-correlation as shown by the negative exponent.

Tables 5 to 7 present the results of MLRs in a similar way to Table 4. The columns of Table 5 contain the exponents of the best fitting $C v_{sw}^{\alpha_1} p_i^{\alpha_2} + D$ models, where $p_i = N_p$, B, etc., and the correlations between models and observations. For example, the first column presents a model in which $\log_{10}C = -7.30$, D =14 pT, $\alpha_1 = 3.28$, $\alpha_2 = 0.48$, and $R = 0.65$. Each column is an independent MLR model.

Table 5 includes MLRs using v_{sw}, which was previously found to be the most important parameter (Table 4), and another parameter. The inclusion of N_p, or any of the other density related parameters, R_{mp} and p_{dyn}, pushes up the correlation coefficient equally to $R = 0.65$, while ϑ_{Bx} and χ have somewhat lower influence. The inclusion of other parameters hardly modifies the result.

We chose N_p as the second parameter. Hence in the MLRs, the results of which are shown in Table 6, v_{sw}, N_p and a third

Table 5. Results of the 2-D MLRs (Pc3ind $= C v_{sw}^{\alpha_1} p_2^{\alpha_2} + D$), and the correlation coefficient, R.

v_{sw}	3.28	2.39	2.44	2.51	2.31	2.33	2.55
N_p	0.49						
B		0.27					
$\cos\vartheta_{Bx}+2$			2.32				
$\cos\chi$				0.18			
R_{mp}					-2.92		
p_{dyn}						0.48	
M_A							0.17
$\log_{10} C$	−7.30	−4.77	−5.63	−4.79	−1.34	−4.60	−5.14
D	14	8	6	5	14	15	6
R	0.65	0.61	0.64	0.63	0.65	0.65	0.61

Table 6. Results of the 3-D MLRs (Pc3ind $= C v_{sw}^{\alpha_1} N_p^{\alpha_2} p_3^{\alpha_3} + D$), and the correlation coefficient, R.

v_{sw}	3.26	3.35	3.30	2.09	3.37	3.28
N_p	0.48	0.58	0.49	−0.11	0.53	0.49
B	0.02					
$\cos\vartheta_{Bx}+2$		2.92				
$\cos\chi$			0.19			
R_{mp}				−3.57		
p_{dyn}					−0.05	
M_A						−0.02
$\log_{10} C$	−7.28	−8.70	−7.25	−0.01	−7.57	−7.30
D	15	12	12	14	14	15
R	0.65	0.71	0.68	0.65	0.65	0.65

Table 7. Results of the 4-D MLRs (Pc3ind $= C v_{sw}^{\alpha_1} p_2^{\alpha_2} (\cos\vartheta_{Bx}+2)^{\alpha_3} \cos^{\alpha_4}\chi + D$, where $p_2 = N_p$ or R_{mp} or p_{dyn}), and the correlation coefficient, R.

v_{sw}	3.36	2.19	2.22
N_p	0.59		
$\cos\vartheta_{Bx}+2$	2.91	2.91	2.93
$\cos\chi$	0.19	0.19	0.19
R_{mp}		−3.52	
p_{dyn}			0.58
$\log_{10} C$	−8.65	−1.46	−5.39
D	9	9	10
R	0.75	0.75	0.75

parameter were used to model Pc3ind. Here the ϑ_{Bx} as a third parameter produced the highest increase in correlation, then $\cos\chi$ follows with an exponent ∼1/5, while neither R_{mp}, nor p_{dyn} is able to further increase the strength of the correlation. The correlation coefficient, however, can be increased further (up to $R = 0.75$) by adding both the cone angle and the solar zenith angle to the parameter set (Table 7).

Similar results to Table 6 can be achieved if we replace N_p by either R_{mp} or p_{dyn} (not shown). In each MLR both the exponent of the third parameter and the correlation strength are very close (within 0.03 and 0.01) to their corresponding values in Table 6. In terms of the MLR model the three density related parameters are interchangeable. For comparison, Table 7 presents the MLR models in which v_{sw}, ϑ_{Bx}, one of the three density related parameters, and a fourth parameter resulting in the highest correlation were considered. The exponent of v_{sw} is different in the different columns, because of its close relation to N_p, R_{mp} and p_{dyn}. The choice of the density related parameter, however, did not influence the exponents of ϑ_{Bx} significantly. In each case χ was found as the fourth most important parameter with the same exponent. Furthermore, the strength of the correlations are the same.

MLRs were also executed separately for each year (Table 8). The results for both the correlation coefficients and the exponents are similar. The exponents of v_{sw}, N_p, $\cos\vartheta_{Bx}+2, \cos\chi$ are about 3, 3/5, 3, 1/5, respectively. In the four parameter MLRs the exponents of R_{mp} and p_{dyn} were found to be around -3 and 1/2 (not shown).

During the period investigated the maximum to minimum ratio of the observed values of v_{sw}, N_p, R_{mp} and p_{dyn} were 4.6, 790, 3.5 and 1702, respectively. However, when determined from the above exponents these ratios change to 97, 55, 43 and 41, characterising the importance of the parameters in the explanation of the variability of the Pc3 index. This result underlines again the priority of v_{sw}, and shows that N_p, R_{mp} and p_{dyn} are about equally important.

In Table 9 the results of four parameters MLRs for other stations are presented (only 2003 data were used). Based on these findings it can be stated that most of the above conclusions are valid also at higher latitudes. There are some differences, however. The role of χ and even ϑ_{Bx} decreases with increasing latitude (decreasing exponent) and, more importantly, the correlation coefficient clearly decreases.

4.4 Artificial Neural Networks

A second method is employed to find the solar wind sources bearing most influence on Pc3ind. We use artificial neural

Table 8. The results of the 4-D MLRs for different years (Pc3ind $= C v_{\mathrm{sw}}^{\alpha_1} N_{\mathrm{p}}^{\alpha_2} (\cos\vartheta_{Bx}+2)^{\alpha_3} \cos^{\alpha_4}\chi + D$).

THY	2001	2002	2003	2004	2005	2006	2007
v_{sw}	2.88	3.20	3.26	3.23	2.48	3.53	3.50
N_{p}	0.57	0.62	0.63	0.60	0.47	0.56	0.56
$\cos\vartheta_{Bx}+2$	2.99	2.93	3.07	3.21	2.31	2.98	2.66
$\cos\chi$	0.23	0.23	0.21	0.17	0.16	0.15	0.14
$\log_{10} C$	−7.34	−8.17	−8.37	−8.41	−5.85	−9.12	−8.92
D	1	5	4	6	7	1	−2
R	0.71	0.74	0.76	0.75	0.69	0.76	0.80

Table 9. The results of the 4-D MLRs, 2003, MM100 stations (Pc3ind $= C v_{\mathrm{sw}}^{\alpha_1} N_{\mathrm{p}}^{\alpha_2} (\cos\vartheta_{Bx}+2)^{\alpha_3} \cos^{\alpha_4}\chi + D$).

2003	THY	BEL	TAR	NUR	HAN	SOD	KIL
v_{sw}	3.26	2.08	2.66	2.85	2.86	2.49	2.70
N_{p}	0.63	0.27	0.48	0.54	0.54	0.46	0.50
$\cos\vartheta_{Bx}+2$	3.07	2.29	2.27	2.35	2.32	1.66	1.56
$\cos\chi$	0.21	0.22	0.18	0.14	0.11	0.06	0.04
$\log_{10} C$	−8.38	−4.22	−6.16	−6.68	−6.73	−5.34	−5.94
D	4	−31	−6	1	2	59	93
R	0.76	0.75	0.65	0.65	0.65	0.46	0.45

networks (ANN's) with various sets of input parameters, similar to those used in the development of the MLR model, to find a set of inputs that optimally model the output parameter, Pc3ind.

Since the use of ANN's is not common in Pc3 studies, we offer a short description of neural networks. For an extensive exploration of the subject, the reader is referred to dedicated texts (e.g. Haykin, 1999; Fausett, 1994; Bishop, 1995).

Artificial neural networks are parallel computational structures, represented by a weighted network of computational nodes, capable of performing complex (non-linear) regression and classification tasks (Haykin, 1999). In this case we use the ANN as a regression model to approximate the output parameter Pc3ind, using a set of input parameters. Multilayer feedforward neural networks (Haykin, 1999), the type we are using, consists of three types of computational nodes: input nodes (comprising the input layer), hidden nodes (which can be collected in multiple hidden layers) and output nodes forming the output layer.

Such an ANN with N input nodes, M hidden nodes in a single hidden layer, and one output node, may be represented by Eqs. (3) and (4) (Bishop, 1995, for example):

$$H_j = f_H\left(\sum_{i=1}^{N}\left[w_{i,j}^{(1)} I_i\right]\right), \quad j \in \{1,\ldots,M\} \tag{3}$$

$$O = f_O\left(\sum_{j=1}^{M}\left[w_j^{(2)} H_j\right]\right) \tag{4}$$

Input nodes I_i are the independent variables and their values are simply the respective sets of input parameter measurements. Hidden nodes H_j apply an activation function f_{H}, usually sigmoidal, and tanh in our case, to the sum of the input parameter values, weighted by $w_{i,j}^{(1)}$. The number of hidden nodes and layers determine the network's ability to resolve highly non-linear behaviour, and are determined by the modeller (Haykin, 1999). The output node computes the approximation to the modelled system by applying a linear activation f_{O} to the sum of the hidden node outputs, weighted by $w_{j,k}^{(2)}$. The output approximating Pc3ind is thus determined by the network as a function of the input parameters and the weights.

The connection weights are determined by the training algorithm, while all other network configuration parameters are fixed by the user. During ANN training the strength of connection weights are iteratively adapted under an optimisation algorithm tasked with minimising the error between modelled and target output values. Network training utilises three distinct sets of input and output parameter measurement data. A training set of input and output data is used to adapt weight strengths during the training process. The validation data set is used to make test predictions of output targets. Upon completion of the training process, the testing data set is used to evaluate the performance of the trained network against unseen input and output data (i.e. data not included in the training or validation sets).

Table 10. Evolution of the wrapper process. Inputs are iteratively added (denoted by x's) according to the performance of the associated network. The set of inputs yielding the highest correlation between measured and modelled output (R) are kept, and the rest of the candidate inputs are varied in the next round of training. Also see Fig. 12.

B_{imf}	x							
N_{p}		x						
v_{sw}			x					
p_{dyn}				x				
M_{A}					x			
ϑ_{Bx}						x		
R_{mp}							x	
$[hrs, hrc]$								x
R	−0.03	0.01	0.51	0.09	0.15	0.35	0.22	0.46
B_{imf}	x							
N_{p}		x						
v_{sw}	x	x	x	x	x	x	x	
p_{dyn}			x					
M_{A}				x				
ϑ_{Bx}					x			
R_{mp}						x		
$[hrs, hrc]$							x	
R	0.50	0.55	0.54	0.50	0.55	0.56	0.76	
B_{imf}	x							
N_{p}		x						
v_{sw}	x	x	x	x	x	x		
p_{dyn}			x					
M_{A}				x				
ϑ_{Bx}					x			
R_{mp}						x		
$[hrs, hrc]$	x	x	x	x	x	x		
R	0.77	0.82	0.83	0.76	0.79	0.82		
B_{imf}	x							
N_{p}		x						
v_{sw}	x	x	x	x	x			
p_{dyn}	x	x	x	x	x			
M_{A}			x					
ϑ_{Bx}				x				
R_{mp}					x			
$[hrs, hrc]$	x	x	x	x	x			
R	0.82	0.83	0.82	0.87	0.83			
B_{imf}	x							
N_{p}		x						
v_{sw}	x	x	x	x				
p_{dyn}	x	x	x	x				
M_{A}			x					
ϑ_{Bx}	x	x	x	x				
R_{mp}				x				
$[hrs, hrc]$	x	x	x	x				
R	0.87	0.87	0.86	0.87				

We set up many ANN's with various sets of input parameters, and evaluate each network, to find a set of input parameters that optimally reproduce the target data set (Sect. 4.4.1). Seven solar wind- and IMF-based parameters are identified, along with two time-based parameters. The sine and cosine of UT hour of the day, $hrs = \sin\left(\frac{2\pi}{24} \cdot \text{hour}\right)$ and $hrc = \cos\left(\frac{2\pi}{24} \cdot \text{hour}\right)$, are included in the set of candidates to model the diurnal variation in Pc3 activity. Employing this pair as input parameters to an ANN is equivalent to using the linear combination $\alpha\, hrs + \beta\, hrc$ as a single input, where the coefficients α and β are just the weights determined by the network training algorithm (see Eq. 3). During training the weights are adapted to optimally reproduce the periodic component of the output parameter. Note that we use hrs and hrc together as a pair of input parameters, since the sine-cosine pair is needed to resolve the periodic component of the output (i.e. so that hour 1 follows after hour 24). The solar wind- and IMF-based candidate input parameters considered are: solar wind speed $v_{\rm sw}$, cone angle ϑ_{Bx}, IMF magnitude $B_{\rm imf}$, solar wind plasma density $N_{\rm p}$, the dynamic pressure, $p_{\rm dyn}$, the magnetopause standoff distance $R_{\rm mp}$, and the Alfvénic Mach number $M_{\rm A}$.

The training set consists of data collected for 2003 (from day 1 to day 365), while the testing data set covers the interval from hour number 1800 to hour number 2500 of 2002, corresponding to about 29 days.

The testing and training sets are reduced by excluding instances where the planetary K index is above 4. This measure is taken to ensure that geomagnetic storm activity is not included in this model. The result is a training data set of 6551 values per parameter (out of a possible 8760 h in the year), while the length of the testing set is 639 (out of 700).

4.4.1 Wrapper process

We employ an ANN wrapper to find the subset of candidate input parameters bearing most influence on the output parameter. A "wrapper" refers to a model dependent feature selection process whereby many models are evaluated and the best performing one selected (e.g. Kim et al., 2005).

Our wrapper is implemented by training and evaluating many ANN's, each with similar configuration, but a different set of input parameters for each network. Every network is trained and evaluated on the data sets described in the previous section. The simulation procedure commences with the training and testing of m ANN's each with a single input parameter ($m = 8$ in this case). The m input parameters are ranked according to each corresponding network's performance. The input parameter corresponding to the best-performing ANN is kept, while the remaining $m-1$ parameters are varied to form $m-1$ pairs of input parameters to be used in the next round of training. The process concludes when all parameters are included as inputs or when the change in network performance due to adding another input parameter stabilises, such that an unambiguous choice is not possible.

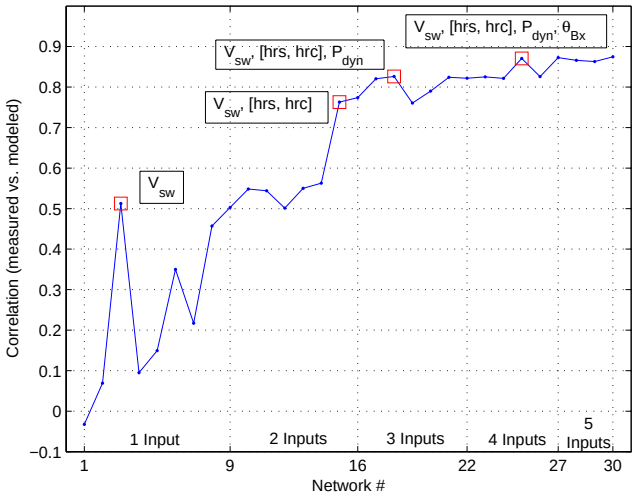

Fig. 12. Correlation between measured and modelled Pc3ind as inputs are added according to the wrapper process. Vertical dashed lines indicate the start of a new round of training. Red squares denote the winner of each round of training, with the corresponding input parameters displayed. See Table 10 for a detailed illustration of the process.

The wrapper process is summarised in Table 10 and illustrated in Fig. 12. Each network is trained using the input parameters marked by x's. The resulting correlation between measured and predicted output is listed in the last row. Figure 12 plots the model performance (correlation between measured and predicted output), versus network trained, as input parameters are varied and added according to the wrapper process. The performance due to each new addition to the optimal set is indicated, and the updated set of inputs listed accordingly. After each round of training a new input is added to the set of influential inputs. After the first round of training, the SW speed emerges as the most influential input for single-input networks. Note that in the wrapper process we treat the time-based pair [hrs, hrc] as a single parameter. The correlation between measured and predicted validation data is $R = 0.51$ for $v_{\rm sw}$. Time [hrs, hrc] and ϑ_{Bx} also yields significant correlation between measured and predicted Pc3ind at $R = 0.46$ and $R = 0.35$, respectively.

In the second round of training, pairs of inputs – $v_{\rm sw}$ and another input from the set of candidates – are used for each network. All pairs of inputs yields prediction accuracy of at least $R = 0.5$. The optimal pair of inputs are the [hrs, hrc] pair and and $v_{\rm sw}$ yielding $R = 0.76$ correlation between measured and predicted output. Other parameters add less to the accuracy of the prediction achieved in the first round – the $v_{\rm sw}$, ϑ_{Bx} pair with $R = 0.55$ and $v_{\rm sw}$, $R_{\rm mp}$ with $R = 0.56$, yielding significant improvement on the first-round results.

The third round of training reveals three sets of inputs yielding near-equal performance: *(i)* $v_{\rm sw}$, [hrs, hrc], $p_{\rm dyn}$ at

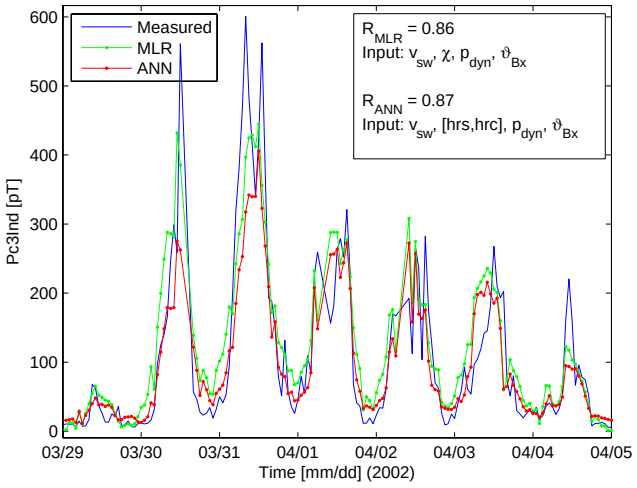

Fig. 13. Measured (solid curve) and modelled (red for ANN and green for MLR model) Pc3ind for a week included in the testing data set, using the optimal set of input parameters as indicated. The correlation between measured and modelled outputs are 0.87 for the ANN and 0.86 for the MLR model.

$R = 0.83$ correlation; *(ii)* $v_{\rm sw}$, $[hrs, hrc]$, $R_{\rm mp}$ at $R = 0.82$; and *(iii)* $v_{\rm sw}$, $[hrs, hrc]$, $N_{\rm p}$ at $R = 0.82$ correlation between measured and predicted Pc3ind. The two best-performing candidates, $p_{\rm dyn}$ and $R_{\rm mp}$, are both directly related to the size of the magnetosphere and the density, $N_{\rm p}$ (along with $v_{\rm sw}$), defines the dynamic pressure. Although the choice is somewhat ambiguous on account of the close separation in correlation coefficients, we select $p_{\rm dyn}$ and continue with the process. The similarity of these three parameters is further illustrated by the correlation between them: calculating the correlation coefficient between the pairs $p_{\rm dyn}$, $N_{\rm p}$ and $p_{\rm dyn}$, $R_{\rm mp}$ over the testing data set yields $R = 0.88$ and $R = -0.78$, respectively. The ANN models are sensitive to this fact, given that subsequent rounds of training do not yield $R_{\rm mp}$ or $N_{\rm p}$ as important – as they do not add any new information to a model with $p_{\rm dyn}$ already included in the set of inputs. As is the case with the MLR models, any one of $R_{\rm mp}$, $N_{\rm p}$ or $p_{\rm dyn}$ could be included at this stage.

We conclude the wrapper process after four rounds of training – with $v_{\rm sw}$, $[hrs, hrc]$, $p_{\rm dyn}$ and ϑ_{Bx} as the final set of influential inputs. The correlation between measured and predicted Pc3ind at this stage is $R = 0.87$. The other sets of inputs all yield accuracy of approximately $R = 0.82$ and do not improve on the previous round's result. A fifth round of training is performed, but no new input is added to the set as no improvement upon the previous round of training is made (see Table 10 and Fig. 12, networks 27 to 30). We conclude that the remaining candidate inputs do not add any new information to the model.

4.4.2 Comparison of MLR and ANN wrapper results

The ANN modelling procedure yields four parameters,

$$v_{\rm sw}, [hrs, hrc], p_{\rm dyn}, \vartheta_{Bx}$$

as the most influential subset of inputs from the candidates. We recall here, that $p_{\rm dyn}$ is interchangeable with $N_{\rm p}$ or $R_{\rm mp}$; the ANN does not prefer one above the others. After four rounds of training, the increase in network performance due to the addition of input parameters is negligible and no further inputs are added.

This result is in agreement with previous studies noting the correlation between $v_{\rm sw}$, ϑ_{Bx} and Pc3 amplitude (e.g. Saito, 1964; Bol'shakova and Troitskaya, 1968; Wolfe, 1980). Furthermore, we know that Pc3 are a largely dayside phenomenon, hence the strong dependence of Pc3ind on the hour of the day. This result is also in accordance with our results based on MLR analysis. Both methods resulted in a four parameter model, in which the density related parameter can be any of $p_{\rm dyn}$, $R_{\rm mp}$, or $N_{\rm p}$.

However, the ANN and MLR results cannot be compared directly. In the MLR analysis we used only dayside data, while in the ANN approach both day and night data were utilised. For the sake of a closer comparison we recalculated the 2003 MLR results for THY including night data. We took first $v_{\rm sw}$ as a model parameter, then added $\cos\chi$, $p_{\rm dyn}$ and $\cos\vartheta_{Bx}$ step by step. The correlation increased gradually, and was $R = 0.42$, 0.69, 0.72 and 0.81, respectively. Note, that we added 2 to $\cos\chi$ and $\cos\vartheta_{Bx}$ to avoid zero and negative values when $\chi >= 90°$ (nightside) or $\vartheta_{Bx} = 90°$, so that log of cos can be taken.

Applying the MLR models inferred from 2003 observations for the test period of ANN (17 March–15 April 2002), the correlation was even higher, $R = 0.49$, 0.76, 0.81 and 0.86, for the different parameter sets, respectively, very close to the ANN correlation values ($R = 0.51$, 0.76, 0.83 and 0.87). Although ANN, as expected, yields a slightly more accurate result, MLR has the advantage that it yields an analytical model. For example, Eq. (5) is the aforementioned four parameter MLR model (based on Eq. 2) obtained from 2003 data as described in Sect. 4.3:

$$\begin{aligned}\text{Pc3ind[pT]} = {} & 4.064 \cdot 10^{-5} v_{\rm sw}^{1.650} \cdot (\cos\chi + 2)^{1.946} \\ & \cdot p_{\rm dyn}^{0.540} \cdot (\cos\vartheta_{Bx} + 2)^{2.675} - 16\,\text{pT}, \end{aligned} \quad (5)$$

where $v_{\rm sw}$ is in $\mathrm{km\,s^{-1}}$, and $p_{\rm dyn}$ in nPa. A comparison of the MLR and ANN models are shown in Fig. 13, for a 7 day period from 29 March to 5 April of 2002. The ANN ($R = 0.87$) narrowly outperforms the MLR model ($R = 0.86$) represented by Eq. (5), employing similar input parameters; the figure illustrates the similarity in performance.

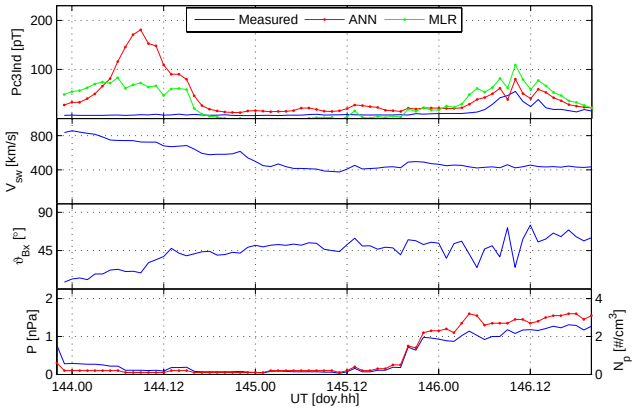

Fig. 14. Measured (solid) and modelled (dotted) Pc3ind during an LDA over 24–26 May 2002 (top panel), along with SW speed (2nd panel), cone angle (3rd panel), and SW dynamic pressure (solid curve, left axis) and plasma density (dotted curve, right axis) in the bottom panel.

4.4.3 Testing the ANN model prediction during low-density events

An LDA on 24–25 May 2002 yielded very low pressure ($p_{\rm dyn} < 0.4$ nPa) and particle count ($N_{\rm p} < 0.3 {\rm cm}^{-3}$) in the SW plasma for most of the 48 h period. Starting from 11:00 UT on 24 May, the solar wind became sub-Alfvénic. In this section we test the MLR (Eq. 5) and ANN (developed in Sect. 4.4.1) models during this LDA event. Input parameter measurements from 24 to 26 May 2002 are used to predict Pc3ind, using both models. Measured Pc3ind is close to zero on 24 and 25 May, with weak activity on the third day.

Figure 14 illustrates the essence of what is described in this section: The top panel of Fig. 14 shows the measured (blue curve) and modelled (MLR – green, ANN – red) Pc3ind for 24–26 May 2002, measured at THY. In the second and third panels $v_{\rm sw}$ and ϑ_{Bx} from OMNI2 are plotted for the same period, respectively. The bottom panel of Fig. 14 depicts the SW dynamic pressure (solid blue line, left-hand axis) and plasma density (dotted red line, right-hand axis) during the interval, also from the OMNI2 set.

On 24 May both models predict moderate pulsation activity – peaking near 90 pT (MLR; Fig. 14, top panel, green curve) and 190 pT (ANN; Fig. 14, top panel, red curve), respectively. Both models appear to react to favourable SW conditions, with $v_{\rm sw} > 600\,{\rm km\,s}^{-1}$ and $\vartheta_{Bx} < 50°$. However, the measured activity (Fig. 14, top panel, blue curve) is very weak at a constant near-zero rate for the entire day along with a very low pressure (bottom panel, blue curve) and density (bottom panel, red curve).

On 25 May SW speed (Fig. 14, second panel) and cone angle (third panel) conditions are less favourable, with the speed decreasing to around 400 km/s and the cone angle increasing to above 50°. The plasma density and dynamic pressure continues at very low levels (below 0.5 particles/cm^3 and 0.5 nPa, respectively). In this case the models react well to the combination of unfavourable speed, IMF direction, and pressure conditions, predicting very low (Pc3ind < 30 pT) activity.

On 26 May some activity is observed (Fig. 14, top panel, blue curve). Solar wind speed remains average, around $400\,{\rm km\,s}^{-1}$ and the cone angle above 40°. The density (pressure) increases step-like from around $0.5\,{\rm cm}^{-3}$ (0.1 nPa) to approximately $3{\rm cm}^{-3}$ (2 nPa) after 18:00 UT on 25 May, remaining near this level for the entire day. In this case both the ANN (red curve) and MLR (green curve) models accurately predict the observed activity – apparently reacting to the increase in pressure, in addition to moderate $v_{\rm sw}$ and ϑ_{Bx} conditions.

Both the ANN and MLR models are sensitive to $v_{\rm sw}$ and ϑ_{Bx} conditions (24–26 May) and to the combination of $v_{\rm sw}$, ϑ_{Bx} and $p_{\rm dyn}$ (25–26 May); however on 24 May, the combination of high SW speed and small cone angle dominates the low pressure and the models incorrectly predict moderate pulsation activity. The insensitivity of the models to extremely low pressure is due to the relative rarity of LDA's with respect to more normal pressure and density conditions in the solar wind. In order for an ANN to correctly model a certain aspect of the modelled system, it must be adequately represented in the training set of data. The fraction of training data set measurements with $p_{\rm dyn} < 1.0$ nPa is 9.8% and only 2% of the data has $p_{\rm dyn} < 0.5$ nPa. The modelling of low-density events could hence be improved increasing the fraction of low-density data in the training set.

5 Discussion

During most of the LDAs and SAEs listed in Tables 2 and 3 the level of Pc3 activity was extremely low (Pc3ind $<$ 10−20 pT, given in the last columns of the tables), and close to the noise level of the instrument (6–7 pT rms in the Pc3 band) which does not coincide with unusually low SW speed or high cone angle. In 6 of 8 LDA events for which dayside Pc3ind values observed at THY were available, ϑ_{Bx} was not more than 50°, and in all cases less than 65°. The same ratios for SAEs were 3 of 6 and 6 of 6. Similarly, $v_{\rm sw}$ was higher than $300\,{\rm km\,s}^{1}$ during all LDAs and during 5 of 6 SAEs for which dayside Pc3 data were available, and higher than $450\,{\rm km\,s}^{-1}$ for half of the LDAs and 1/3 of the SAEs. These solar wind conditions are not unfavourable, and in some cases decidedly favourable for UW generation.

We also investigated some events in more detail. There were no observable Pc3s during an LDA on 16 February 2004 (see Fig. 1), during the course of a SAE on 13 September 2004 (Fig. 2), and the previous long-lasting LDA as presented in Sect. 3.2. In another case on 24 May 2002 (Fig. 14) analysed in Sect. 4.4.3, the Pc3 activity ceased for two days, in spite of the high $v_{\rm sw}$ and moderate cone angle. Similarly,

Le et al. (2000a) found that during the LDA+SAE of May 1999 Pc3s were absent, although the IMF cone angle was favourable (∼40°) for UW generation, and v_{sw} was moderately low (350 km s^{-1}).

During LDAs the magnetosphere calms and the upstream interplanetary region may become quiet. E.g. during the May 1999 LDA event Smith et al. (2001) and Le et al. (2000a) reported one order of magnitude decrease of the ULF wave activity in the ion-foreshock. During the rarefaction interval, the rms of B_{imf} underwent a factor of 5–10 reduction (0.1–0.2 nT) compared to the fluctuations in the neighbouring plasma (1 nT). Smith et al. (2001) explained this behaviour by the refraction of fast-mode ULF waves away from the regions where the Alfvén speed is high. We prefer an alternative explanation, that is, since there were practically no protons present in the foreshock the generation of upstream ULF waves through wave-particle interaction would be much weaker. Le et al. (2000a) raised the idea that extremely low Mach number (M_{ms}) could be responsible for the pause in ULF activity in May 1999. They supposed that the low Mach number shock reflected very few particles. They also emphasised that a potential effect of the Mach number should be separated from the dependence of the activity on v_{sw}.

We demonstrated by statistical analysis that beside v_{sw} and ϑ_{Bx}, N_p or another solar wind density related parameter also has a key role in the control of dayside Pc3 activity. Both MLR and ANN analyses ranked N_p more important than ϑ_{Bx}. Earlier works have already raised the possibility that N_p may play some role, however, its influence from other SW parameters had not yet been separated. A similar strong dependence in the low-density range was also found by Verő (1980) at $L = 1.9$ in the 50–200 mHz band whenever N_p was lower than 5 cm^{-3} (the lowest bin used in that study was $0-5$ cm^{-3}) and by Chugunova et al. (2007) in the Pc3 band at auroral and near-pole latitudes (for $N_p < 2$ cm^{-3}). At higher N_p values the Pc3 amplitudes slowly decreased with increasing SW density. This tendency can be clearly observed in our results (Fig. 3), as well. Verő (1980) also found that the N_p dependence was strong in the same frequency bands where the implicit v_{sw} dependence suggests that this relation is just a consequence of the interdependence of these parameters. Wolfe and Meloni (1981) realised that after v_{sw} and ϑ_{Bx}, N_p is the third parameter that has a significant effect on ground (17–33 mHz) pulsations at $L = 3.5$. All of these results imply that N_p has a similar role at low, medium and high latitudes, thus suggesting a common source of dayside Pc3s over large regions. However, none of the cited authors interpreted their results in depth.

To our knowledge the dependence of Pc3 activity on other density related parameters, except for flux density and dynamic pressure has not been investigated. Here we demonstrated a relationship with the Alfvénic and magnetosonic Mach number, with the SW dynamic pressure, and with the standoff distance of the magnetopause. We also showed that N_p, p_{dyn} and R_{mp} are equally important and interchangeable parameters in MLR and ANN empirical models. In the following we give a physical interpretation of the found relations.

There are several possibilities of how N_p may affect surface Pc3 activity:

1. In the absence of upstream protons, ULF waves cannot be generated. Upstream ULF waves gain their energy from back scattered SW particles via the ion-cyclotron mechanism (e.g. Gary, 1978; Yumoto et al., 1984; Le and Russell, 1994; Heilig et al., 2007b). Fewer particles mean less energy to be transferred during wave-particle interactions. This may be one of the reasons why there are no Pc3s when N_p is extremely low (< 2 cm^{-3}). It would appear that the SW proton density acts as an "on-off" switch for mid-latitude dayside Pc3s, in the sense that under moderate N_p the Pc3 amplitude is governed mostly by the SW speed, IMF direction (ϑ_{Bx}) and local time as on 26 May (Fig. 14). However, under very low proton counts (24, 25 May), Pc3 activity disappears regardless of otherwise favourable SW plasma conditions. This agrees with data in Fig. 3, where Pc3 activity ceases for number densities below 2 cm^{-3}, while above this threshold, the density only weakly influences Pc3 amplitude.

2. When N_p is low the bow shock may become weak (i.e. M_A is low), hence the protons are reflected back less efficiently (Thomsen et al., 1993; Kucharek et al., 2004), which can lead to the decrease of upstream ULF wave activity (Le et al., 2000a). Onsager et al. (1990) and Thomsen et al. (1993) found that there is a definite tendency for the beams of near-specular reflected ions to be absent at the lower (< 5) Mach numbers. Without reflected ions, upstream waves will not be generated.

3. As the SW flow becomes sub-Alfvénic ($M_A < 1$), upstream ULF waves that are propagating upstream at the Alfvén speed in the plasma frame (Yumoto et al., 1984; Narita et al., 2004; Heilig et al., 2007b) are not efficiently convected back downstream toward the shock, and cannot enter the magnetosphere. Thus UWs are not able to act as a source of ground Pc3 activity under sub-Alfvénic conditions.

4. Low plasma density results in larger standoff distance of the bow shock and the magnetopause nose, i.e. the ULF waves have to propagate over a longer path to reach the ionosphere and the ground. If there is some kind of damping present in the magnetosphere it could explain the observed amplitude reduction. During the famous 1999 event the Earth's bow shock was crossed by the Wind spacecraft as far as 53 R_E in radial distance from the Earth, as reported by Le et al. (2000b). ULF wave propagation in the magnetosphere is usually interpreted in the frame of the magnetohydrodynamic (MHD) theory. Since MHD is lossless, MHD waves propagate

without damping. Therefore, in the MHD frame one can only count on geometric effects, e.g. the exponential decay of the evanescent mode (Takahashi et al., 1994). Compressional mode waves can propagate in any direction. Supposing a point-like source (e.g. the subsolar point of the magnetopause) and spherical wave fronts compressional waves will suffer attenuation with a factor of $1/r$, where r is the distance from the source, as a consequence of spatial spreading of the wave front. This type of attenuation is called geometric attenuation. We found, however, a much stronger exponential decay as shown in Fig. 4. The attenuation can be given in the form $\mathrm{Pc3ind} = \mathrm{Pc3ind}_0 e^{-\lambda r}$, where $\mathrm{Pc3ind}_0$ is the the amplitude index at $r_0 = 1\ R_\mathrm{E}$. In the case of THY the apparent attenuation factor λ is 0.32, meaning that 50% ($(e^{-0.32})^2 \approx 0.53$) of the wave energy is lost at $dr = 1\ R_\mathrm{E}$ distance. The real attenuation can be smaller, since as we showed in Fig. 10, after we had normalised Pc3ind with v_sw the attenuation became close to linear, decreasing Pc3ind with 16 pT at $dr = 1\ R_\mathrm{E}$ distance. Further studies and multipoint observations in the magnetosphere are needed to find the real attenuation factor, its location, and the physical processes responsible.

Although all four of the scenarios described above are possible and can be responsible for the disappearance of Pc3s during LDAs, none of them has been discussed in detail or verified using empirical data prior to this study.

We also derived empirical models that can be used to predict Pc3 amplitudes at any local time. The model parameters for THY and other MM100 stations are given in Tables 7, 8 and 9. In spite of the obvious SW density dependence incorporated in the models it cannot account for the disappearance of Pc3s at LDAs and SAEs as was shown in Sect. 4.4.3. The reason for this may be that there is more than one mechanism at work, simultaneously. Mechanism 2 is supported by direct foreshock observation of the decrease of wave energy during a SAE (Le et al., 2000a). However, we think that mechanism 1 can also be responsible. More foreshock observations are needed to discriminate between these possibilities. Mechanism 3 should also act as a switch for UW related Pc3 activity according to UW theory. Mechanism 4, the attenuation of ULF wave energy with distance, should act continuously and we think that this phenomenon is the source of the sensitivity of our models on the variation of N_p. This is the only mechanism of the four that has a strong effect over the range of measurements observed. Mechanisms 1, 2 and 3 seem to be important under conditions of extremely low N_p.

We found that the roles of χ and ϑ_{Bx} in controlling Pc3ind to decrease with increasing latitude as can be concluded from the decreasing correlations seen in Table 9. It implies that mid latitude ($L = 1.8 - 3.8$) Pc3 activity is more tightly linked to the UWs than that at higher latitudes. This fact can be a result of a low latitude (e.g. subsolar) source, but it can also mean that there are other dayside Pc3 sources at higher latitudes not controlled or controlled but in a different way by the considered parameters.

The upstream wave source mechanism is only one of the ways the solar wind can drive dayside magnetospheric ULF waves. The decelerated solar wind plasma flowing in the magnetosheath may generate surface waves on the flanks of the magnetopause via the Kelvin-Helmholtz instability. Kelvin-Helmholtz waves which have a typical time scale of a few minutes (i.e. in the Pc4-Pc5 band) in turn may couple to internal resonances inside the magnetopause as realized first in the 1970s by Southwood (1974); Chen and Hasegawa (1974). As a consequence of the generation mechanism, Kelvin-Helmholtz waves are more intense at high SW speeds (similar to UW generated Pc3's), but also have a dawn and a dusk peak in the local time distribution of their power, unlike the power of UW generated Pc3's, that peaks around local noon.

The SW dynamic pressure fluctuations (and frozen-in magnetic field) can also be a source of dayside compressional ULF waves. Kepko et al. (2002) have shown that ULF waves at discrete frequencies (0.4–3 mHz) are sometimes directly driven by density oscillations present in the undisturbed ambient solar wind.

Pressure pulses in the solar wind may cause impulsive compressions of the magnetosphere, capable of exciting broad band compressional waves in the magnetosphere which can couple to cavity (Kivelson and Southwood, 1985; Lee and Lysak, 1989) or waveguide (Samson and Rankin, 1994) modes. We should note, however, that observational evidence for global fast mode cavity resonance or waveguide mode is still very limited (Samson and Rankin, 1994; Waters et al., 2002).

Beside these external sources, internal disturbances can also lead to wave generation. E.g. irregularly shaped 7–25 mHz waves referred to as Pi2s are clearly linked to substorm activity (e.g. Saito et al., 1976).

Pc3–Pc5 pulsations can be observed everywhere in the magnetosphere, generally as a superposition of externally or internally driven waves and the resonant response of the magnetosphere. Previous works (e.g. Verő, 1980; Wolfe and Meloni, 1981; Wolfe et al., 1985; Chugunova et al., 2007) have demonstrated that although under strong SW control, Pc3, Pc4 and Pc5 pulsations react differently to changes in SW conditions, possibly due to their different origins. Pc2s (100–200 mHz) are very rarely observed at mid latitudes (Saito, 1969; Anderson et al., 1992). Thus, although the band of UWs covers also the higher part of the Pc4 range, we restricted our study to Pc3s, to avoid unnecessary mixing of physical phenomena which could have "contaminated" our result.

Pc3 amplitudes at low and mid latitudes are modified by local resonances. In the highly inhomogeneous magnetosphere the incoming compressional waves couple to shear Alfvén mode, and drive field line resonances where their

frequencies match the local eigenfrequencies. The ground Pc3 activity is a mixture of the remnant of the incoming UW related source and the neighbouring field line resonances. The resonant amplification takes place at varying frequency, because the eigenfrequency of the field line at a given location varies with the magnetospheric density (e.g. Schulz, 1996; Waters et al., 1996), which in turn is controlled by geomagnetic activity. The IMF strength also changes with time. Moreover, both the field line resonance frequency and the frequency of the driving UWs (which depends on the IMF strength) has a significant solar cycle variation (Verő, 1996), that makes the situation more complicated. The amplification caused by the resonance has a smaller effect on the average amplitudes compared to the SW parameters investigated. The role of the field line resonance in redistributing the incoming ULF energy was not considered in our models.

The Pc3 amplitude is further modified by the ionospheric screening described e.g. by Nishida (1978) or Pilipenko et al. (2008). The controlling factor in screening is the Hall to Pedersen conductance ratio. This ratio is considered to be relatively stable (e.g. Juusola et al., 2007), so it is not expected to cause large Pc3 amplitude modulation. Nevertheless, neither this effect nor the winter anomaly of Pc3 pulsations described by Verő et al. (1995) were considered in our Pc3 activity models.

We demonstrated through the two models developed here that the upstream solar wind controls dayside Pc3 activity. Since Pc3s may be measured by ground-based magnetometers, the Pc3 activity level may be used as a proxy for some solar wind conditions, especially in the event of satellite or satellite-communications malfunction. The idea put forward by Verő (1975) to calculate v_{sw} from pulsation indices might be explored further.

6 Conclusions

It was clearly demonstrated that Pc3s cannot be observed on the ground during sub-Alfvénic periods or during LDAs. These findings strongly support the upstream origin of dayside Pc3s at mid latitudes. This result also means that N_p is one of the key parameters controlling ground Pc3 activity.

We showed that the empirical models of ground Pc3 pulsation activity can be significantly improved by the inclusion of N_p or some other density dependent parameter, especially the standoff distance of the magnetopause or the dynamic pressure. The dependence of Pc3 amplitudes on M_{ms} and M_A, as well as on the standoff distance of the nose of the magnetopause were all presented here for the first time.

The dependence of ground Pc3 on local time is demonstrated and well understood. The time-derived inputs, especially when data from all local times were considered, contributed significantly to the modelled Pc3ind data. However, the empirical models could not reconstruct the extremely low or ceasing Pc3 activity during LDAs.

We note here that our Pc3 index cannot discriminate between Pc3s and Pi activity in the same frequency band. Although daytime Pi2s are regularly observed at low latitudes, they are brief, impulsive events and would not influence the 1-h averaged data used in the development of the models. Our models suppose a single source, namely the UW activity, although there are more than one source in the Pc3 band. Our results show that UWs are the dominant source of dayside Pc3 activity.

The disappearance of Pc3s during low-density solar wind events can have at least four causes according to the existing UW theory: 1. Pausing the ion-cyclotron resonance that generates the upstream ULF waves in the absence of protons, 2. Weakening of the bow shock that implies less efficient reflection, 3. The solar wind becomes sub-Alfvénic and hence it is not able to sweep back the waves propagating upstream with the Alfvén-speed, and 4. The increase of the standoff distance of the magnetopause (and of the bow shock). Our analysis supports UW activity as the dominant source of mid-latitude Pc3s. The UWs at higher latitudes, beyond the plasmapause, seem to have a relatively small contribution. Future models should include other sources, as well.

The correlation between the considered parameters can be different at different time scales. We will investigate this scale dependence based on higher time (1 min) resolution data. We expect that the cone angle dependence will be stronger at shorter time scales, since it can change very rapidly. Future models should also take into account the possible time lags between the controlling parameters and the Pc3 activity response.

Instead of mixing bands (Pc2–4), we could develop individual models for a variety of frequency bands, not necessarily determined by pulsation classes, and compare the various driving mechanisms responsible for activity within those bands. This is beyond the scope of this particular investigation, however, but may be pursued in the future.

The models presented here may augment other pulsation index applications, such as the Pc3 pulsation index predictions made by the Australian Space Weather Agency (http://www.ips.gov.au). Specifically, an investigation into the residual error made in the prediction of Pc3ind values may yield insight into the role of other pulsation generation mechanisms. Since only solar wind parameters are used as input parameters to these models, some components of the error may be interpreted as the influence of other physical mechanisms not considered by our models, such as field line resonances and other internal magnetospheric parameters. In this sense, we may view the models developed here as prototypes and this investigation as a "proof-of-concept" to motivate the further development of the models introduced here.

Acknowledgements. This research was supported by the Hungarian Space Office, grant TP 153, the Hungarian Scientific Research Fund (K 75640) and a South African-Hungarian bilateral project funded by the Hungarian Science and Technology Foundation (OMFB-00300/2008) in Hungary and the National Research Foundation in

South Africa. The OMNI data were obtained from the GSFC/SPDF OMNIWeb interface at http://omniweb.gsfc.nasa.gov.

Topical Editor R. Nakamura thanks F. W. Menk and another anonymous referee for their help in evaluating this paper.

References

Anderson, B. J., Erlandson, R. E., and Zanetti, L. J.: A model of the Earth's distant bow shock, J. Geophys. Res., 97, 3089–3101, 1992.

Bishop, C. M.: Neural Networks for Pattern Recognition, Oxford University Press, 1995.

Bol'shakova, O. V. and Troitskaya, V.: Relation of the IMF direction to the system of stable oscillations, Dokl. Akad. Nauk+ (Proceedings of the Russian Academy of Sciences), 180, 343–346, 1968.

Chen, L. and Hasegawa, A.: A theory of long-period magnetic pulsations, 1. Steady state excitation of field line resonance, J. Geophys. Res., 79, 1024–1032, 1974.

Chi, P., Russell, C., Bloom, R., and Singer, H.: Solar wind control of ultralow-frequency wave activity at L=3, J. Geophys. Res., 103, 29467–29477, 1998.

Chugunova, O. M., Pilipenko, V. A., Engebretson, M., and Rodger, A.: Statistical Relations between the Probability of Occurrence of Pc3-4 Pulsations at High Latitudes in the Antarctic Regions and the Solar Wind and IMF Parameters, Geomagn and Aeronomy+, 47, 205–215, 2007.

Fausett, L.: Fundamentals of Neural Networks: architectures, algoritms and applications, Prentice Hall, 1994.

Gary, S. P.: Electromagnetic ion beam instability and energy loss of fast alpha particles, Nucl. Fusion, 18, 327, 1978.

Greenstadt, E. W. and Olson, J. V.: Pc 3,4 Activity and Interplanetary Field Orientation, J. Geophys. Res., 81, 5911–5920, 1976.

Haykin, S.: Neural Networks: A Comprehensive Foundation, Pearson Education, 2nd edn., 1999.

Heilig, B., Csontos, A., Pankratz, L., Pajunpää, K., Kultima, J., Raita, T., Reda, J., and Váczyová, M.: Upstream wave related Pc3 pulsations observed by the MM100 meridional magnetometer array, Publications of the Institute of Geophysics of the Polish Academy of Sciences, C-99, 339–346, 2007a.

Heilig, B., Lühr, H., and Rother, M.: Comprehensive study of ULF upstream waves observed in the topside ionosphere by CHAMP and on the ground, Ann. Geophys., 25, 737–754, doi:10.5194/angeo-25-737-2007, 2007b.

Hundhausen, A., Bame, S., Asbridge, J., and Sydoriak, S.: Solar Wind Proton Properties: Vela 3 Observations from July 1965 to June 1967, J. Geophys. Res., 75, 4643–4657, 1970.

Juusola, L., Amm, O., Kauristie, K., and Viljanen, A.: A model for estimating the relation between the Hall to Pedersen conductance ratio and ground magnetic data derived from CHAMP satellite statistics, Ann. Geophys., 25, 721–736, doi:10.5194/angeo-25-721-2007, 2007.

Kepko, L., Spence, H. E., and Singer, H. J.: ULF waves in the solar wind as direct drivers of magnetospheric pulsations, Geophys. Res. Lett., 29, 1197, doi:10.1029/2001GL014405, 2002.

Kim, Y., Street, W. N., Russell, G. J., and Menczer, F.: Customer Targeting: A Neural Network Approach Guided by Genetic Algorithms, Manage. Sci., 51, 264–276, doi:10.1287/mnsc.1040.0296, 2005.

Kivelson, M. G. and Russell, C. T.: Introduction to space physics, Cambridge University Press, London, 1995.

Kivelson, M. G. and Southwood, D. J.: Resonant ULF waves: A new interpretation, Geophys. Res. Lett., 12, 49–52, 1985.

Kovner, M. S., Lebedev, V. V., Plyasova-Bakunina, T. A., and Troitskaya, V. A.: On the generation of low frequency waves in the solar wind in front of the bow shock, Planet. Space Sci., 24, 261–267, 1976.

Kucharek, H., Möbius, E., Scholer, M., Mouikis, C., Kistler, L. M., Horbury, T., Balogh, A., Rème, H., and Bosqued, J. M.: On the origin of field-aligned beams at the quasi-perpendicular bow shock: multi-spacecraft observations by Cluster, Ann. Geophys., 22, 2301–2308, doi:10.5194/angeo-22-2301-2004, 2004.

Kulcar, L.: Long-term variations of the solar wind density – velocity relation, Contrib. Astron. Obs. Skalnaté Pleso, 17, 21–36, 1988.

Le, G. and Russell, C. T.: The morphology of ULF waves in the Earth's foreshock, in: Solar wind sources of magnetospheric ultra-low-frequency waves, pp. 87–98, Geophysical Monogr. 81, AGU, Washington, D.C., 1994.

Le, G., Chi, P. J., Goedecke, W., Russell, C. T., Szabo, A., Petrinec, S. M., Angelopoulos, V., Reeves, G. D., and Chun, F. K.: Magnetosphere on May 11, 1999, the day the solar wind almost disappeared: II. Magnetic pulsations in space and on the ground, Geophys. Res. Lett., 27, 2165–2168, 2000a.

Le, G., Russell, C. T., and Petrinec, S. M.: The magnetosphere on May 11, 1999, the day the solar wind almost disappeared I. Current systems, Geophys. Res. Lett., 27, 1827–1830, 2000b.

Lee, D. H. and Lysak, R. L.: Magnetospheric ULF wave Coupling in the Dipole Model: the Impulsive Excitation, J. Geophys. Res., 94, 17097–17103, 1989.

McComas, D. J., Barraclough, B. L., Funsten, H. O., Gosling, J. T., Santiago-Munoz, E., Skoug, R. M., Goldstein, B. E., Neugebauer, M., Riley, P., and Balogh, A.: Solar wind observations over Ulysses' first full polar orbit, J. Geophys. Res., 105, 10419–10433, 2000.

Miyake, W., Mukai, T., Yumoto, K., Saito, T., and Hirao, K.: A Correlation Study between the Solar Wind Speed Observed by Suisei and the Amplitude of Pc 3 Geomagnetic Pulsations, J. Geomagn. Geoelectr., 39, 159–164, 1987.

Narita, Y., Glassmeier, K.-H., Schäfer, S., Motschmann, U., Fränz, M., Dandouras, I., Fornaon, K.-H., Georgescu, E., Korth, A., Rème, H., and Richter, I.: Alfvén waves in the foreshock propagating upstream in the plasma rest frame: statistics from Cluster observations, Ann. Geophys., 22, 2315–2323, doi:10.5194/angeo-22-2315-2004, 2004.

Nishida, A.: Geomagnetic diagnosis of the magnetosphere, Springer, New York, 1978.

Onsager, T. G., Thomsen, M. F., Gosling, J. T., Bame, S. J., and Russell, C. T.: Survey of Coherent Ion Reflection at the Quasi-Parallel Bow Shock, J. Geophys. Res., 95, 2261–2271, 1990.

Pilipenko, V., Fedorov, E., Heilig, B., and Engebretson, M. J.: Structure of ULF Pc3 waves at low latitudes, J. Geophys. Res., 113, A11208, doi:10.1029/2008JA013243, 2008.

Saito, T.: A new index of geomagnetic pulsation and its relation to solar M-regions, Rep., Ionos. Space Res., Japan, 18, 260–274, 1964.

Saito, T.: Geomagnetic pulsations, Space Sci. Rev., 10, 319–412, 1969.

Saito, T., Yumoto, K., and Koyama, Y.: Magnetic pulsation Pi2 as

a sensitive indicator of magnetospheric substorm, Planet. Space Sci., 24, 1025–1029, 1976.

Samson, J. C. and Rankin, R.: The coupling of solar wind energy to MHD cavity modes, waveguide modes, and field line resonances in the Earth's Magnetosphere, in: Solar wind sources of magnetospheric ultra-low-frequency waves, pp. 253–264, Geophysical Monogr. 81, AGU, Washington, D.C., 1994.

Schulz, M.: Eigenfrequencies of geomagnetic field lines and implications for plasma-density modeling, J. Geophys. Res., 101, 1738517397, 1996.

Smith, C. W., Mullan, D. J., Ness, N. F., M.Skoug, R., and Steinberg, J.: Day the solar wind almost disappeared: Magnetic field fluctuations, wave refraction and dissipation, J. Geophys. Res., 106, 18625–18634, 2001.

Southwood, D. J.: Some features of field line resonances in the magnetosphere, Planet. Space Sci., 22, 483–491, 1974.

Takahashi, K. B., Anderson, B. J., Newell, P. T., Yamamoto, T., and Sato, N.: Propagation of compressional Pc3 pulsations from space to the ground: a case study using multipoint measurements, in: Solar wind sources of magnetospheric ultra-low-frequency waves, pp. 355–363, Geophysical Monogr. 81, AGU, Washington, D.C., 1994.

Thomsen, M. F., Gosling, J. T., Onsager, T. G., and Russell, C. T.: Ion and Electron Heating at the Low-Mach-Number, Quasi-Parallel Bow Shock, J. Geophys. Res., 98, 3875–3888, doi: 10.1029/92JA02560, 1993.

Usmanov, A. V., Goldstein, M. L., Ogilvie, K. W., Farrell, W. M., and Lawrence, G. R.: Low-density anomalies and sub-Alfvénic solar wind, J. Geophys.Res., 110, A01106, doi:10. 1029/2004JA010699, 2005.

Verő, J.: Determination of the solar wind velocity from pulsation indices, J. Atmos. Terr. Phys., 37, 561–564, 1975.

Verő, J.: Geomagnetic pulsations and parameters of the interplanetary medium, J. Atmos. Terr. Phys., 42, 371–380, 1980.

Verő, J.: Solar cycle effect on Pc 3 geomagnetic pulsations, J. Geophys. Res., 101, 2461–2465, 1996.

Verő, J., Best, I., Vellante, M., Lühr, H., de Lauretis, M., Holló, L., Märcz, F., and Střeštik, J.: Relations of field line resonances and upstream waves and the winter attenuation of pulsations, Ann. Geophys., 13, 689–697, doi:10.1007/s00585-995-0689-4, 1995.

Veselovsky, I. S., Dmitriev, A. V., and Suvarova, A. V.: Algebra and Statistics of the Solar Wind, Cosmic Res., 48, 115–130, 2010.

Waters, C. L., Samson, J. C., and Donovan, E. F.: Variation of plasmatrough density derived from magnetospheric field line resonances, J. Geophys. Res., 101, 2473724745, 1996.

Waters, C. L., Takahashi, K., Lee, D.-H., and Anderson, B. J.: Detection of ultralow-frequency cavity modes using spacecraft data, J. Geophys. Res., 107, 1284, doi:10.1029/2001JA000224, 2002.

Wolfe, A.: Dependence of mid-latitude hydromagnetic energy spectra on solar wind speed and interplanetary magnetic field direction, J. Geophys. Res., 85, 5977–5982, 1980.

Wolfe, A. and Meloni, A.: ULF geomagnetic power near L=4. 6. Relationship to upstream solar wind quantities, J. Geophys. Res., 86, 7507–7512, 1981.

Wolfe, A., Meloni, A., Lanzerotti, L. J., and MacLennan, C. G.: Dependence of hydromagnetic energy spectra near L=2 and L=3 on upstream solar wind parameters, J. Geophys. Res., 90, 5117–5131, 1985.

Yedidia, B. A., Vellante, M., Villante, U., and Lazarus, A. J.: A study of the relationship between micropulsations and solar wind properties, J. Geophys. Res., 96, 3465–3470, 1991.

Yumoto, K., Saito, T., Tsurutani, B. T., Smith, E. J., and Akasofu, S.-I.: Relationship between the IMF magnitude and Pc 3 magnetic pulsations in the magnetosphere, J. Geophys. Res., 89, 9731–9740, 1984.